

MASTER THESIS

# Dissolved Ionic Salts under Nanoconfinement

Institute for Theoretical Physics

Utrecht University  
Utrecht

Author  
Sebastian Bielfeldt



First Reviewer  
Prof. Dr. René van Roij  
Institute for Theoretical Physics  
Utrecht University  
Utrecht

Second Reviewer  
Prof. Dr. Marjolein Dijkstra  
Debye Institute for Nanomaterials Science  
Utrecht University  
Utrecht

Utrecht, 10 July 2022

# Dissolved Ionic Salts under Nanoconfinement

Sebastian Bielfeldt

January 2022

## Abstract

Since the first isolation of graphene barely twenty years ago, quasi two-dimensional structures have been investigated in great detail as their properties such as their relative permittivity and heat conductivity vary greatly from the macroscopic three dimensional (bulk) case. More recently, dilute electrolyte solutions confined in nanoscale slits have been observed to form clusters at ambient conditions and a theoretical framework for describing this phenomenon based on a quasi two-dimensional Coulombic interaction (Q2D) has been developed. Using classical molecular dynamics simulations (MD), we found that sodium chloride (NaCl) as well as a generic, divalent salt dissolved in water showed that the electric current per ion is not strongly affected by the applied electric field but decreases with increasing ionic density, due to increased cluster formation. For a range of salts, including LiCl, NaCl, CaSO<sub>4</sub> and CaCl<sub>2</sub>, analysis of the potentials of mean forces (PMF) shows that dissolved cations and anions in nanoslits attract each other more strongly than in the bulk case. Comparing the PMFs with the Q2D calculations, we find that they match well in the long range limit. However, at distances of a few angstroms, we show that Q2D fully neglects excluded volume effects and that its predictions for highly charged ions (valence Z=2) deviate from the effective interactions extracted by our MD simulations.

## Acknowledgments

I am extremely grateful to Prof. Dr. René van Roij and Marjolijn Dijkstra for their great guidance and feedback. Many thanks to Giuliana Giunta and Gerardo Campos Villalobos for the countless hours of advice, patience and support. Also, I extend my sincere thanks to Bas Wensink, Vladimir Denk, Úna Parkinson, and Leon Goertz for their all-seeing eyes and piercing questions.

## Contents

<b>1</b>	<b>Introduction</b>	<b>1</b>
<b>2</b>	<b>Theory</b>	<b>4</b>
2.1	Interatomic Potentials . . . . .	4
2.2	Salts and Electrolytes . . . . .	5
2.3	Diffusion . . . . .	6
2.4	The Effect of Nanoconfinement . . . . .	7
<b>3</b>	<b>Model and Methods</b>	<b>9</b>
3.1	Molecules . . . . .	10
3.2	Time Integration . . . . .	11
3.3	Nosé-Hoover Thermostat . . . . .	13
3.4	Grand Canonical Simulations . . . . .	14
3.5	Ewald Summation . . . . .	15
3.6	Walls . . . . .	17
3.7	Potential of Mean Force . . . . .	18
<b>4</b>	<b>Results and Discussion</b>	<b>23</b>
4.1	Attaching a Water Reservoir . . . . .	23
4.2	Diffusion . . . . .	26
4.3	Constant Electric Field . . . . .	28
4.4	Potential of Mean Force . . . . .	31
<b>5</b>	<b>Conclusion</b>	<b>40</b>
<b>A</b>	<b>Measure of Accuracy: R-squared</b>	<b>I</b>
<b>B</b>	<b>Different Orientations of Calcium Sulfate</b>	<b>I</b>
<b>C</b>	<b>Comparing PMFs</b>	<b>II</b>
<b>D</b>	<b>Pressures</b>	<b>IV</b>
<b>E</b>	<b>Additional Figures</b>	<b>VI</b>
	<b>References</b>	<b>IX</b>

## 1 Introduction

Whether atomically thin materials such as two-dimensional (2D) crystals can exist was a topic of debate almost a century ago. Many scientists, including Lev Landau, such crystals were considered not to exist in a free state and their description solely an academic exercise [1, 2]. For decades, their study was a purely theoretical and computational undertaking. This changed when twenty years ago Andre Geim and Kostya Novoselov isolated graphene for the first time [3], earning them the Nobel prize a mere six years later. It was the first time a 2D crystal had been realized in an experimental setting. In graphene, electrons turn into massless relativistic particles which need to be described by the 2+1 Dirac Equation [4]. It is a material that is flexible yet extraordinarily rigid with the highest elastic constants ever measured in any material and, even at a single layer's width, it is highly impermeable to gases [5]. The isolation of graphene sparked a boom in research of not just graphene, but two-dimensional materials in general. Soon, other 2D crystals were isolated such as hexagonal boron nitride (hBN) and molybdenum disulfide (MoS<sub>2</sub>). While they share some of their properties with graphene, in other regards they differ. What they have in common is that they gain a range of features in the single-layer – two-dimensional – case compared to the case of several layers stacked on top of each other.

This in turn generated interest in combining different 2D materials. In the last few years, complicated heterostructures joining graphene, hBN, were made as well as structures combining 2D and 3D elements. For example, two-dimensional channels can be fabricated by fusing two atomically flat 3D crystals together with graphene layers at the edges keeping them a few angstroms apart. The opening between the two graphene layers represents the thinnest channel one can currently build with atoms. By choosing different spacers, for example, another 2D crystal or an aforementioned combination of several crystals, one can create slits of various widths on an angstrom level scale, an example of a graphene double-layer separating two blocks of graphite is shown in Fig. 1 [6]. With such nanoscale slits, the study of gases and liquids under nanoscale confinement or nanoconfinement becomes possible.

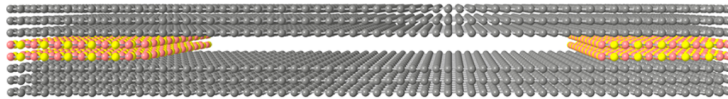


**Figure 1: Illustration of a nanoslit.** Example of an angstrom-scale cavity built with a 3 dimensional, atomically flat wall and a 2-dimensional, double layer spacer, both made of carbon. Image taken from Ref. [6]

Water, just like 2D crystals, arranges itself in layers and loses some properties characteristic of 3D water, if inserted in slits thinner than 2 nm (nanoslits)[7]. These slits were shown to allow gases and liquids to pass through very quickly – more so than expected according to the current theoretical interpretation (Knudsen diffu-

sion). This was explained by the atomically flat nature of the slits [8]. For example, in the out-of-plane dimension, its dielectric constant is reduced. At a specific combination of slit height and density, water was even observed to form a crystalline sheet at room temperature [7]. At slit heights of 0.7 nm or two graphene layers, one can build slits through which water molecules fit yet larger particles don't. This means nanoslits can perform reverse osmosis, filtering for example ions out of salt water.

In the 3D bulk case, many ions such as sodium chloride (NaCl) dissolve in water. When inserted a nanoslit, however, we observe that they form pairs or clusters. In molecular dynamics (MD) simulations, it was shown that ions inserted in a single water layer quickly formed large clusters. In long-running experiments, it was shown that 50 ns after randomly distributing ions across a slit, NaCl had formed rectangular crystals and lithium chloride (LiCl) rings and/or chains [9]. In both cases, all ions were part of some cluster at the end of the simulation. Nonetheless, clustering was observed on shorter time scales and wider slits, too.

More interesting properties of such slits were seen by adding an electric field to the nanoconfined electrolytes. MD simulations showed that the ions can be captured while water flows through the slit when an electric field was applied in the out-of-plane directions [10]. This provides another way to achieve reverse osmosis. Furthermore, an electric field acting on oppositely charged particles applies forces pointing in opposite directions. Indeed, pairs are pulled apart, if an electric field parallel to the plane of a nanoslit is sufficiently strong. However, the application of an electric field increases rather than reduces cluster formation for various salts for a wide range of electric fields [11]. For most materials, one observes Ohm's law, which states that the current is proportional to the electric field (the black line in Fig. 2). But the formation of clusters affects the resulting electric current, as the contribution of a pair of oppositely charged ions perfectly cancels (assuming a 1:1 salt). Therefore, the current depends on the share of free ions, that is ions that are not part of a pair or cluster. The higher the share of free ions, the stronger the current, all else being equal. However, as the electric fields influence the share of free ions, the current displays a non-linear response to an in-plane electric field. As a consequence, these nanoconfined electrolytes do not observe Ohm's law.

The height of such slits is crucial for their conductive behavior. The conductivity of NaCl in a slit approaches that of NaCl in the bulk at widths between just 2 and 3 nm, [12]. At slit heights of more than 1 nm, one sees alternating layers of anions and cations, given sufficient space, also separated by water. These channels serve as transport channels and can thus improve conductivity. For widths of 2 nm or more, one sees that at most four layers (i.e. peaks in concentration) appear. In the middle of the slit, a homogeneous structure forms rather than more peaks [12, 13].

Clusters do not form instantaneously but instead, take a finite amount of time to form. Consequently, a change in the external electric field affects the conductivity with a delay. Therefore, different currents can be measured for the same electric field depending on which electric field was applied shortly before. In other words, a nanoconfined electrolyte displays a form of memory, which makes this system part

of a class of electronic devices called memristors (a portmanteau of memory and resistor). When applying an oscillating electric field, we see that the current forms a pinched hysteresis loop whereas for a system without memory we would observe a single current for each electric field (this argument is also illustrated in Fig. 2). The most pronounced memristive behavior, which is the biggest difference between the upper and lower branch of the current, is the largest for nanoconfined electrolytes at frequencies ranging from  $10^3$  to  $10^6$  Hz. Memristors have applications in a wide range of systems such as memory storage and neuromorphic computing. In a Brownian dynamics study, memristors built from several nanoconfined electrolytes were used to simulate the spiking pattern of a neuron [11].

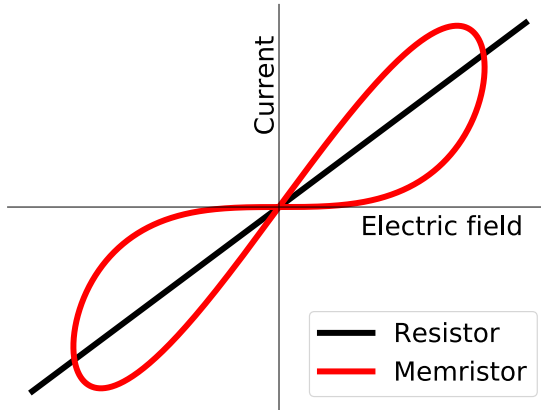


Figure 2: **Resistor vs memristor.** Illustration of an oscillating electric field is applied to an Ohmic resistor and a non-Ohmic memristor.

Considering the many interesting properties and applications of 2D materials in general and nanoconfined electrolytes in particular, we set out to better understand ions dissolved in nanoscale slits. In chapter 2, we establish a shared understanding of the matter at hand by revising some concepts about ions, their interaction, diffusion, and currents. We then present a recently developed analytical description of confined ions. In chapter 3, we will define the system that we research and give an introduction to the molecular dynamics techniques that we used to implement time evolution, and heat baths as well as how we modeled the interactions between ions. In chapter 4, we present our results. We find that high pressures are required to insert water or an electrolyte into a single layer slit. Then, we show that the rate of diffusion, as well as conductivity, decreases for both monovalent and divalent ions with ion concentration under nanoconfinement. Furthermore, we calculate effective interactions for a range of ion pairs and find the valence to dominate the strength of the interaction in the long-range as well as exacerbating short-range effects due to the finite size of water. In chapter 5, we present the main conclusions.

## 2 Theory

### 2.1 Interatomic Potentials

If atoms come very close to each other, their electron orbitals overlap. This forces some electrons into energetically less favorable states, as not more than two electrons can exist in the same orbital due to the Pauli exclusion principle. This, in turn, creates a strong, repelling force. At distances of a few angstroms, the electron distributions do not overlap anymore, yet the fluctuations in electron positions in one atom still affect the electron positions in other atoms. This results in a net attractive force, which is described by the derivative of the London dispersion potential (also the London-van der Waals potential). This potential scales with  $r^{-6}$  compared with the inter-particle distance  $r$  [14]. Taken together, these two effects allow for a fairly realistic description of atomic interaction. The Lennard-Jones (LJ) potential is a computationally efficient implementation of this in the case of two identical point-like particles which are surrounded by a repelling soft shell with an effective diameter  $\sigma$ . Then, the LJ potential with the well depth of  $-\epsilon$  is

$$V_{\text{LJ}}(r) = 4\epsilon \left[ \left(\frac{\sigma}{r}\right)^{12} - \left(\frac{\sigma}{r}\right)^6 \right]. \quad (2.1)$$

The interaction becomes attractive at a distance of  $2^{1/6}\sigma$  yielding a potential of  $-\epsilon$  which corresponds to the total net attraction  $\int_{2^{1/6}\sigma}^{\infty} V_{\text{LJ}}(r) dr$ . Whereas the second term is derived from the London dispersion potential, the first one is chosen for computational convenience (while still being accurate)<sup>1</sup>. Many similar potentials are replacing the  $(\sigma/r)^{12}$  with different large polynomials, exponentials, and other quickly decreasing functions.

As stated before, the LJ potential is defined as the interaction between two specific particles. However, one can approximate the LJ parameters of different particles using only the LJ parameters of their respective self-interactions. Lorenz and Berthelot showed that using only the parameters of the particle interacting with itself, one determines the cross parameters by taking the arithmetic average of the diameters [15] and the geometric average of the well depth [16]. In theory, all particle-particle interactions need to be calculated. However, the largest term of the LJ potential is of  $\mathcal{O}(r^{-6})$ . For distances of single-digit multiples of  $\sigma$ , the contributions of the LJ potential are already insignificant fractions of  $\epsilon$ , irrespective of the density distribution of the system. Therefore, one can introduce a cutoff distance  $r_{\text{cut}}$  to avoid unnecessary calculations.

Simplicity and computational efficiency combined with fairly realistic results lead to the LJ potential being one of the most popular potentials to model atom and molecule interaction – from the early days of computer simulation physics to this day.

---

<sup>1</sup>Computers are very quick at taking the square of a value (such as  $((\sigma/r)^6)^2$ ) – much faster than taking something to the power of 11 or 13/6.

Ions are electrically charged atoms, i.e. the number of electrons present doesn't match the atomic number of the atom. Not being charge neutral, their interaction cannot be summarized by the Lennard-Jones potential alone. The  $i$ th and  $j$ th ion are also affected by the electric interaction of their respective charges  $q_i$  and  $q_j$  as described by the Coulomb potential

$$V_C(r) = \frac{1}{4\pi\varepsilon_0\varepsilon_R} \frac{q_i q_j}{r}. \quad (2.2)$$

Here,  $\varepsilon_0$  and  $\varepsilon_R$  denote the permittivity of the vacuum and the relative permittivity of the material, respectively. For the case that one considers charges in just two dimensions, the corresponding potential can be obtained by integrating over the third dimension, yielding

$$V_{2DC}(r_{ij}) = \frac{q_i q_j}{4\pi\varepsilon_0\varepsilon_R} \log \frac{r_{ij}}{L}, \quad (2.3)$$

where the length scale  $L$  can be chosen to fix the potential.

## 2.2 Salts and Electrolytes

Salts consist of a combination of cations and anions, i.e. positively and negatively charged ions, respectively. Macroscopically, a salt is charge neutral. They are held together by ionic bonds where the anion effectively receives electrons from the cation. The number of electrons an ion shares or receives is referred to as valence  $Z$ . In water, electrons move from the hydrogen atoms towards the oxygen atoms and are effectively shared between both through a covalent bond. This change in charge distribution creates a dipole within the water molecule. If one inserts a salt such as sodium chloride (NaCl) in water, the polar water molecules bind to the ions. If the ions dissociate from each other to form bonds with water molecules instead, this solution is referred to as an electrolyte. Salts are differentiated by the valence of their anions and cations. Salts such as NaCl or lithium chloride LiCl are monovalent/univalent (or more concisely 1:1) as both anion and cation have a valence of one. With the same reasoning, calcium chloride CaCl<sub>2</sub> is considered univalent (2:1) and calcium sulfate CaSO<sub>4</sub> divalent (2:2) salt.

A common measure of how many ions are inserted in an electrolyte is the ion concentration  $c$ . It is defined as the number  $N$  of salt molecules which are inserted in a certain volume  $V$  yielding

$$c = \frac{N}{N_A V} \quad (2.4)$$

with the Avogadro constant  $N_A$ . A solvent cannot dissolve infinite quantities of salt. The maximum level of ion concentration is referred to as solubility. At higher concentrations, not all salt molecules will be dissolved. For example in the case of NaCl dissolved in water, solubility is reached at an ion concentration of 6.2 mol/l at 298 K [17].

When one applies an electric field to an electrolyte, ions experience the electrostatic force. Cations move in – and anions opposite to – the direction of the electric

field. The rate at which they move can be determined via the electric current  $I$ . It measures the flow of charges through a given cross-sectional area  $A$  and can macroscopically be measured by summing over all ion species  $j$  traveling at an average speed of  $v_j$  along the electric field and volumetric particle density  $N_j/V$  yielding  $I = A \sum_{j \in \{+, -\}} \frac{N_j}{V} q_j v_j$ .

In our simulation, we measure the current microscopically and thus rearrange the equation to fit our needs. Dividing  $V/A$ , we obtain the length  $L$  along which the electric field  $\mathbf{E}$  is applied with strength  $E$  and obtain

$$I = \left\langle \frac{1}{L} \sum_{i=1}^N q_i \frac{\mathbf{r}_i(t) - \mathbf{r}_i(t - \Delta t)}{\Delta t} \right\rangle \cdot \frac{\mathbf{E}}{E}. \quad (2.5)$$

To determine whether an electrolyte behaves like an Ohmic conductor, it is useful to look at another quantity, the conductivity. This measures the electric current flowing through a given cross sectional area  $A$  at an electric field  $E$ , yielding

$$\sigma = \frac{1}{A} \frac{I}{E}. \quad (2.6)$$

### 2.3 Diffusion

As we saw with the current in the previous section, we can gain a lot of interesting information from the average velocity of a particle. Yet in some systems, there is simply no movement, while in others particles move quickly but without a preferred direction. In both cases, the average velocity is zero even though the systems differ a great deal. A way to differentiate between the two is by calculating the square of the average change in position  $\mathbf{r}_i(t)$  between a starting time  $t_0$  and a final time  $t$  for all  $N$  particles and  $i \in (1, N)$ . This gives us the mean squared displacement  $R^2(t)$  of particles as

$$R^2(t) = \frac{1}{N} \sum_{i=1}^N (\|\mathbf{r}_i(t) - \mathbf{r}_i(t_0)\|)^2 \quad (2.7)$$

As particles meander in the diffusive regime and move in all directions, they display a linear relationship between the time and  $R^2(t)$  [18]. On the contrary, if the average particle were to move in a specific direction at a constant speed, we would see a quadratic relationship between the particles'  $R^2(t)$  and the time. In the case of a diffusive regime, we can use the slope of  $R^2(t)$  to quantify how much particles move. Therefore, we introduce the diffusion constant  $D$  which for a given dimension  $d$  equals

$$D = \frac{R^2(t)}{2d(t - t_0)}. \quad (2.8)$$

In the case of charged ions, we can use  $D$  to measure the conductivity  $\sigma$ . For a dilute salt, this can be done by rewriting the Nernst-Einstein equation (NE) [12]. The Nernst-Einstein equation connects  $D$  and  $\sigma$  by combining the species  $j$  specific

quantities for the number of ions  $N_j$ , their charge  $q_j$  and their diffusion constant  $D_j$  with the  $T$  the temperature,  $k_B$  the Boltzmann constant and  $V$  the volume, yielding

$$\sigma_{\text{NE}} = \frac{1}{V k_B T} \sum_{j \in \{+, -\}} N_j q_j^2 D_j. \quad (2.9)$$

This will allow us to compare the currents measured at given electric fields with the rate of diffusion that we measure without an electric field present.

## 2.4 The Effect of Nanoconfinement

As stated in the introduction, water arranges itself in layers under nanoconfinement. The structure of water in the confined dimension differs greatly from the 3D bulk case. This has direct consequences on the conductive properties of water. The in-plane dielectric coefficient  $\varepsilon_{||}$  of water is essentially the same as the isotropic dielectric coefficient of the bulk case  $\varepsilon_{\text{bulk}} = 80$ . The dielectric coefficient in the out-of-plane direction,  $\varepsilon_{\perp}$ , was measured to be 2 for slit widths smaller than 1.5 nm (and smaller than 20 for widths of 10 nm) [19]. Over short distances, the strength of the interactions scales with the geometric mean of the in-plane and out-of-plane dielectric coefficients (i.e.  $\sqrt{\varepsilon_{\perp} \varepsilon_{||}}$ ) [11].

The dielectric coefficient of graphene is around 2, varying slightly under different conditions [20]. This is comparable to other atomically flat insulating walls and very low compared to  $\varepsilon_{||}$  in the slit. This changes the shape of the electric field of a charge placed in the water. Consider a point charge at the center of the slit; it will be surrounded by an electric field which can be split into a radial in-plane and an out-of-plane component,  $E_{||}$  and  $E_{\perp}$  respectively. For  $E_{||} \gg E_{\perp}$ , the Coulomb potential is effectively two-dimensional. To determine up to which distance this is roughly the case, consider a cylinder around such a point charge, with some radius  $\xi$  and a height  $h$  equal to the width of the slit. Flux conservation demands that

$$2\pi\xi h \varepsilon_{||} E_{||} \approx 2\pi\xi^2 \varepsilon_m E_{\perp} \quad (2.10)$$

with  $\varepsilon_m$  the dielectric coefficient of the confining material. Rearranging of this relationship yields  $\xi = h \frac{\varepsilon_{||}}{\varepsilon_m} \frac{E_{||}}{E_{\perp}}$ . The component  $E_{||}$  corresponds to the interaction of two particles in the slit, whereas  $E_{\perp}$  represents the potential reaching through the walls of the slit. At the transition of the two regimes, the electric field becomes almost isotropic i.e.  $E_{||} \approx E_{\perp}$ . Thus, the transition between two- and three-dimensional behavior occurs at

$$\xi = h \frac{\varepsilon_{||}}{\varepsilon_m}. \quad (2.11)$$

For distances smaller than  $\xi$ , the field lines remain within the confined slit and thus behave effectively as in the two-dimensional regime. One function which scales with  $\log r$  for small  $r$  and with  $\frac{1}{r}$  for larger distances is  $\log \frac{r}{r+r_{\text{trans}}}$  where  $r_{\text{trans}}$  is the point where the shift between the two regimes occurs. This can easily be checked by looking at the first nonzero term of the Taylor approximation for  $r \gg r_{\text{trans}}$  and  $r \ll r_{\text{trans}}$ .

With this reasoning as well as a more in-depth analytical calculation, a recent paper [11] proposed the following effective Coulomb potential experienced by two point charges

$$\beta V_{Q2D}(r) = -\frac{q_i q_j}{T^*} \log \left( \frac{r}{r + \xi} \right) \quad (2.12)$$

where

$$T^* = \frac{2\pi\epsilon_0\epsilon_{||}h}{1.1Z^2e^2}k_B T$$

with 1.1 being a leftover of the approximations and  $\xi$  defined as in Eq. (2.11). If we use  $\epsilon_m = 2$ , we find that the effective Coulomb potential is in the logarithmic regime up to a distances of  $\xi = 14\text{ nm}$ . In chapter 4.4, we will look at how well this theory predicts interaction within the logarithmic regime.

A measure of the relative strength of thermal fluctuations within a solvent compared to the electrostatic potential is given by the Bjerrum length  $\lambda_B$ . It is defined as  $\beta V_C(\lambda_B) = 1$  for a 1:1 electrolyte, yielding the following distance at which there is an equilibrium between the electrostatic and thermodynamic potential,

$$\lambda_B = \frac{\beta e^2}{4\pi\epsilon_0\epsilon_R}. \quad (2.13)$$

An electrolyte has been shown to experience phase separation between ions and solvent if the diameter of the ions is smaller than  $\frac{1}{16}\lambda_B$  [21]. In such cases, ions form structures instead of binding to the water. For mono- and divalent ions dissolved in bulk water at room temperature,  $\lambda_B$  is around 0.7 and 2.8 nm, respectively. Therefore, the distance at which pairs form is of order 0.1 nm and thus shorter than the diameter of the repulsive core of any atom, effectively prohibiting the formation of pairs. Therefore, this leads to the above-mentioned dissolution in water.

In nanoscale slits, as discussed in the previous section, ions are arranged into layers, just like the smaller water molecules. As discussed above, the electric permittivity of such a slit system is lower than in the bulk case. The change in permittivity increases the  $\lambda_B$  by a factor of six. On top of that, the electric field doesn't behave three-dimensionally at such length scales. Instead, it has a quasi-two-dimensional shape, further increasing the electrostatic forces in the in-plane surface. The resulting Bjerrum length ( $\beta V_{Q2D}(\lambda_B^{Q2D}) = 1$ ) for monovalent ions equals  $\lambda_B^{Q2D} = 130\text{ nm}$  which is 100 times larger than the three-dimensional bulk case. Hence, the Coulombic forces between dissolved cations and anions are extremely attractive in nanoconfinement [11].

### 3 Model and Methods

For all simulations, we use the software package Large-scale Atomic/Molecular Massively Parallel Simulator (LAMMPS) [22]. We primarily perform molecular dynamics (MD) simulations for which we will now detail our setup. We are interested in the behavior of an electrolyte under nanoconfinement. We insert a range of ionic salts, together with water, into two kinds of systems: the (nano-)slit as our system of interest as well as a periodic bulk system as a control. To analyze the behavior in the bulk, we use a cubic box of edge length  $L$  with periodic boundary conditions in all directions. In the case of the slit, we still maintain periodicity in the  $x$ - and  $y$ -direction and keep  $L_x = L_y$  (with  $L_x$  being 10 nm, unless otherwise specified). As explained in the previous section, the quasi 2D Coulomb (Q2D) potential predicts that the Coulomb interactions scale logarithmically for a range of up to  $\xi = 14 \text{ nm}$ . This means this regime extends for more than one box length. Larger box sizes were not feasible due to computational costs. In the  $z$ -dimension, there are repulsive walls that are placed a distance  $h$  apart. They are either uniform or resemble a graphene layer and repel all other particles in this simulation. This will be further discussed in chapter 3.6. For the most part, we choose the slit height  $h$  to be 1 nm. This corresponds to a single layer of ions and two layers of water. While we also look at a slit (NaCl) in a single layer of water as have others [12, 9], there are doubts whether any electrolyte will enter a single layer slit [6, 10]. Other salts certainly do not fit in such thin slits [11]. To have more comparability we thus focus on a system with two layers of water.

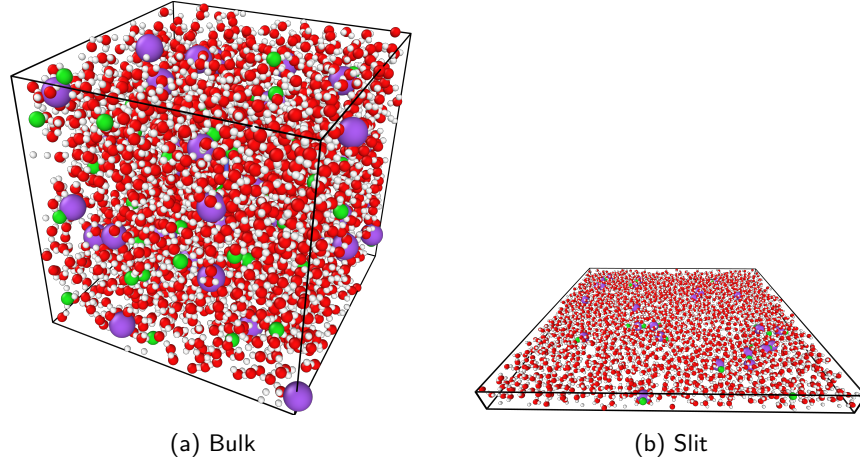


**Figure 3: Illustrations of a bulk system and a slit system.** (a) We show a bulk system with side length  $L = 4 \text{ nm}$ . (b) The slit has an edge lengths  $L_x = 10 \text{ nm} = L_y$  and slit height  $h = 1 \text{ nm}$ .

In this system, we want to insert a range of ionic salts such as sodium chloride

(NaCl), calcium sulfate (CaSO<sub>4</sub>), calcium chloride (CaCl<sub>2</sub>) and lithium chloride (LiCl). Furthermore, to analyze the effect that a change of charge has, we also create a generic salt with the LJ parameters of sodium chloride but higher valence. We sometimes refer to those generic (fictitious) versions of sodium chloride as bivalent ( $Z = 2$ ), and trivalent ( $Z = 3$ ) salt – in direct comparison, actual sodium chloride is then referred to as monovalent. We list all relevant properties to describe the interactions between all atoms and molecules in our simulation, specifically their charge, mass, and LJ parameters, in Tab. 1. The interaction between different ions are governed by Lorentz-Berthelot mixing rules as explained in the chapter 2.

Atom Types	Charge $q$ [e]	Mass $m$ [g/mol]	Diameter $\sigma$ [\AA]	Well depth $\epsilon$ [ $\frac{\text{kcal}}{\text{mol}}$ ]	Ref.
Na <sup>+</sup>	+1.000	22.990	2.350	0.123	[11]
Na <sup>+</sup> (alt.)	+1.000	22.990	3.328	0.002 77	[9]
Cl <sup>-</sup>	-1.000	35.453	4.401	0.100	[11, 9]
Li <sup>+</sup>	+1.000	6.941	2.026	0.0183	[9]
Ca (CaSO <sub>4</sub> )	+2.000	40.078	2.895	0.100	[11]
S (CaSO <sub>4</sub> )	-1.000	32.065	3.550	0.250	[11]
O (CaSO <sub>4</sub> )	-1.000	15.999	3.150	0.200	[11]
H	+0.424	1.0	0.0	0.0	[11]
O (H <sub>2</sub> O)	-0.848	15.999	3.165	0.155	[11]
C	0.0	12.011	3.214	0.057	[11]

Table 1: Overview over interaction parameters of different atoms

In the following, we will detail the techniques underpinning our simulations. We first describe how we can reduce the number of calculations by reducing the degrees of freedom of atoms that are part of a molecule. Then, we present the different algorithms necessary to simulate different ensembles. Additionally, we introduce a method to properly calculate the Coulomb potential in a periodic system and how to apply this to partially periodic systems. Lastly, we discuss two common techniques to analyze the effective interaction potentials of materials in a solvent.

### 3.1 Molecules

Molecules are a combination of atoms that experience the same fundamental forces as “free” atoms. However, the forces pulling them together are so much stronger compared to other forces that their degrees of freedom are effectively reduced. In simulations, one wants to minimize the number of calculations while maintaining the underlying mechanics of the system. Interactions of the individual atoms within a molecule are therefore simplified by leveraging the fact that the forces holding molecules together are orders of magnitude stronger than other forces in the system. At its extreme, such bonds essentially dictate the relative position. Then, we can model them as a single unit with fixed angles and distances from their center of mass. For example, in our description of SO<sub>4</sub> ions where we fix the oxygen atoms to lie at an angle (109.5°) to all other oxygen atoms and a fixed distance of 1.47 Å to the sulfur atom.

In other cases, atoms are attached to each other yet they have still some freedom

to move. An example of this is the model we used for the water molecules in this work. We model water by using the extended simple point charge model (SPC/E) [23] as the basis for their relative positions and charges. It assigns charges to all three atoms yet only to oxygen nonzero LJ parameters, as well as placing them on the vertices of? an isosceles<sup>2</sup> triangle with a fixed angle. The distance at which hydrogen atoms reside respective to the oxygen atoms is not fixed unlike in the case of calcium sulfate. Instead, they can vibrate, which we implement by attaching a harmonic potential between the oxygen and hydrogen atoms. There is a whole class of algorithms, so-called constraint algorithms, to efficiently solve these extra potentials. They achieve computational efficiency by neglecting less relevant degrees of freedom. In this case, the hydrogen bonds in our simulation were maintained rigid with the SHAKE algorithm [24]. We can use it to speed up our calculations as we are not interested in the exact nature of the vibrations of the hydrogen atoms w.r.t the oxygen atoms.

When making such approximations, we need to keep in mind that they only hold under certain assumptions. Hydrolysis, the process in which water molecule bonds break, sets in at voltages above 1.23 V [25]. Furthermore, in the ionic bonds that the molecules form, electrons move from one nucleus closer to others, effectively changing the charges of individual atoms. This can even lead to changes in the LJ parameters from the literature value of the free case, which is why there are two different values given for oxygen in Tab. 1.

### 3.2 Time Integration

In statistical mechanics, the behavior of large microscopic entities is studied to measure macroscopic quantities by discovering the properties of the average state of the system. One core tenet of statistical mechanics is the ergodic hypothesis. It states that the average over all possible states, the ensemble average, and the average over time should be the same. The underlying assumption is that any state can transition to any other state given enough time. This assumption doesn't always hold and is virtually impossible to prove for larger systems, yet it is commonly assumed for processes such as diffusion. The ergodic hypothesis is useful as time evolutions are a lot easier to calculate than initializing many independent configurations. Therefore, time evolutions are interesting not only for time-dependent but also for time-independent processes. To do this, we split our time frame into many small time steps and determine the next position for each of the  $N$  particles of the system. For this, we add up all forces acting on the particle  $i$  and calculate the acceleration of the particle as

$$m_i \ddot{\mathbf{x}}_i = -\nabla V_{\text{System}}(\mathbf{x}_i(t + \Delta t), \mathbf{x}^N(t + \Delta t),). \quad (3.1)$$

Those forces we express as the potentials  $V_{\text{System}}$ , dependent on all particles  $k \in (1, N)$  positions  $\mathbf{x}_k$  at time  $t$ . The  $i$ th particle is thus not only affected by its own position in the system but also by the position of all other particles  $\mathbf{x}^N = \mathbf{x}_1, \dots, \mathbf{x}_N$

---

<sup>2</sup>A triangle with two sides of equal length.

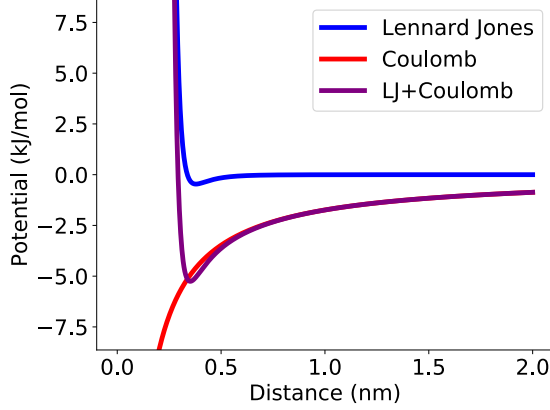


Figure 4: **LJ and Coulomb interaction of NaCl pair** with respect to their distance.

present in the system<sup>3</sup>. Its position in the system determines the forces that the walls apply to it. We model the interaction with other particles through so-called force fields also referred to as additive pair potentials, specifically the Coulomb and LJ potential. The relative permittivity is equal to one since we simulate all particles explicitly.

The position and velocity we can simply store and look up (at least after the first time step). Thus, we have access to the zeroth, first and second derivative of position and can use those to calculate the particle's next position. This process is called time integration. One implementation of this is the Verlet algorithm [26]. Consider the Taylor approximations of a particle's position  $\mathbf{x}_i$  up to third order one time step before and after the current time

$$\mathbf{x}_i(t + \Delta t) = \mathbf{x}_i(t) + \dot{\mathbf{x}}_i \Delta t + \frac{1}{2} \ddot{\mathbf{x}}_i(t) \Delta t^2 + \frac{1}{6} \dddot{\mathbf{x}}_i(t) \Delta t^3 + \mathcal{O}(\Delta t^4) \quad (3.2)$$

$$\mathbf{x}_i(t - \Delta t) = \mathbf{x}_i(t) - \dot{\mathbf{x}}_i \Delta t + \frac{1}{2} \ddot{\mathbf{x}}_i(t) \Delta t^2 - \frac{1}{6} \dddot{\mathbf{x}}_i(t) \Delta t^3 + \mathcal{O}(\Delta t^4). \quad (3.3)$$

By adding the two together, one obtains

$$\mathbf{x}_i(t + \Delta t) = 2\mathbf{x}_i(t) - \mathbf{x}_i(t - \Delta t) + \ddot{\mathbf{x}}_i(t) \Delta t^2 + \mathcal{O}(\Delta t^4). \quad (3.4)$$

This is a very elegant algorithm that reduces calculation errors to the 4th order of the time step. At the same time, it requires only the previous two positions plus the acceleration  $\mathbf{a}_i$  of (i.e., the forces applied to) a particle. A drawback of this algorithm is that one does not obtain positions and velocities at the same time. Instead one obtains velocities for every  $t + \frac{1}{2}\Delta t$ . As a consequence, additional calculations

---

<sup>3</sup> $i$  is included here, too, as the  $i$ th particle can interact with itself through periodic boundary conditions

are necessary to obtain speeds and positions at the same time. Furthermore, one always needs the two previous positions. This means that for the first time step of a simulation velocities need to be known or inferred, potentially leading to different runs based on the same input data [27].

One way to remedy this issue is a variation of this algorithm called velocity Verlet [28]. This is done by explicitly inserting the velocity  $\mathbf{v}_i(t)$  into Eq. (3.4). Now, one also has to calculate the velocity, leading to a total of three steps (assuming that the  $\mathbf{a}_i(t)$  does not depend on  $\mathbf{v}_i(t)$ ). First, one calculates the next position  $\mathbf{x}_i(t)$  for all particles by

$$\mathbf{x}_i(t + \Delta t) = \mathbf{x}_i(t) + \mathbf{v}_i(t)\Delta t + \frac{1}{2}\mathbf{a}_i(t)\Delta t^2. \quad (3.5)$$

Using the new position, one calculates the acceleration of all particles at time  $t + \Delta t$ . Then one uses this to calculate the velocity at the next time step by

$$\mathbf{v}_i(t + \Delta t) = \mathbf{v}_i(t) + \frac{\mathbf{a}_i(t) + \mathbf{a}_i(t + \Delta t)}{2}\Delta t. \quad (3.6)$$

To summarize this algorithm, for each particle we first calculate the next position  $\mathbf{x}_i(t + \Delta t)$  via Eq. (3.5), then the acceleration  $\mathbf{a}_i(t + \Delta t)$  via Eq. (3.1) and lastly the next velocity  $\mathbf{v}_i(t + \Delta t)$  via Eq. (3.6). This we then do for all particles at every time step. Now, we calculate velocities and positions at the same time. This is useful, for example, to check energy conservation, as it is crucial to calculate potential and kinetic energy at the same time which depends on positions and velocities, respectively [27]. With this information, we can fully implement the microcanonical ensemble, i.e. a system where both the number of particles  $N$  and the amount of energy  $E$  are conserved. Also, the size of the system is held fixed meaning that we have a constant volume, too. A shorthand way to refer to a given statistical ensemble is by naming the quantities held constant giving us the *NVE* ensemble. Now we move on to see how other ensembles can be realized.

### 3.3 Nosé-Hoover Thermostat

While fairly straightforward to calculate in a simulation, a microcanonical ensemble is harder to obtain in experiments. Energy is fairly hard to measure directly, whereas constant heat is easier to realize. In a canonical system, heat is exchanged with a heat bath to obtain a thermal equilibrium at constant temperature  $T$  instead of constant  $E$ . Therefore, we now speak of an *NVT* ensemble. The Nosé-Hoover thermostat is a molecular simulation tool to analytically emulate the effect of a heat bath at constant  $T$ . It uses an extra variable  $s$  coupled to the velocities, leading to a modified Hamiltonian

$$\mathcal{H} = \sum_{i=1}^N \frac{\mathbf{p}_i^2}{2m_i s^2} + V(r^N) + \frac{p_s^2}{2Q} + Lk_B T \ln s, \quad (3.7)$$

where  $Q$  represents an effective mass associated with  $s$  and  $L$  a parameter that one fixes later to a convenient value. In total, it depends on  $N$  positions  $\mathbf{x}_i$  and  $s$  as well

as their respective momenta, leading to a total count of  $6N + 2$  degrees of freedom. This Hamiltonian, the sum of potential and kinetic energy, is not conserved. We want to fix the temperature, rather than the overall energy, so this is the desired outcome in an  $NVT$  ensemble. From this Hamiltonian, we can derive the following equations of motion

$$\frac{d\mathbf{x}_i}{dt} = \mathbf{p}_i/m_i \quad (3.8)$$

$$\frac{d\mathbf{p}_i}{dt} = \frac{\partial V(\mathbf{x}_i^N)}{\partial \mathbf{x}_i} - \epsilon \mathbf{p}_i \quad (3.9)$$

$$\frac{ds}{dt} = \epsilon \quad (3.10)$$

$$\frac{d\epsilon}{dt} = \frac{1}{s} \left( \sum_{i=1}^N p_i^2/m_i - \frac{L}{\beta} \right), \quad (3.11)$$

with  $\epsilon = sp_s/Q$  and  $p_s$  the momentum of  $s$ . For these equations, instead of  $\mathcal{H}$ , there exists another conserved quantity  $\mathcal{H}'$  defined as

$$\mathcal{H}' = \sum_{i=1}^N \frac{\mathbf{p}_i^2}{2m_i s^2} + V(r^N) + \frac{p_s^2}{2Q} + Lk_B T \ln s. \quad (3.12)$$

It is however not a Hamiltonian since the equations of motion cannot be derived from it. One can then use  $\mathcal{H}'$  to monitor that the heat bath is working as intended. For their derivation from the above given  $\mathcal{H}$ , consult Ref. [27, p. 152].

### 3.4 Grand Canonical Simulations

In a grand canonical system, we have not just a thermal but also a chemical equilibrium. Instead of keeping the number of particles constant, we fix the chemical potential  $\mu$  which is the change in energy obtained through releasing a particle into the system. In keeping with the naming scheme, the shorthand for this system is  $\mu VT$ . One way to simulate such a system is to use a Monte Carlo algorithm, i.e., randomly “proposing” changes to the system and accepting/rejecting them based on a rule. When performing grand canonical simulations with Monte Carlo (GCMC), this would be the insertion, removal as well as translation of particles. One algorithm that does this is the Metropolis algorithm which compares a function of the energy of the system with a random number between zero and one. When applied to grand canonical systems, one formulation of the Metropolis algorithm describes the probabilities at which molecules are inserted as

$$p_{\text{ins}} = \min \left[ 1, \frac{1}{1 + \frac{\Lambda^3(N+1)}{V \exp(\beta\mu)} \exp(\beta(E_{t+1} - E_t))} \right], \quad (3.13)$$

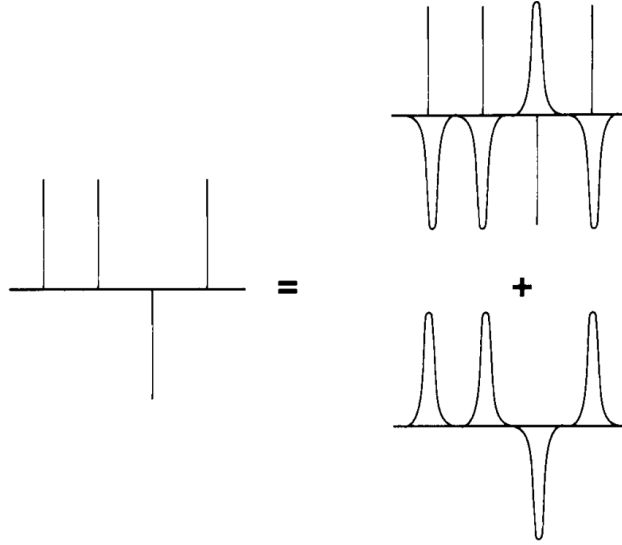


Figure 5: **Example of Ewald approach.** For every point charge, one adds two normally distributed charge densities (one positive and one negative) with the same overall charge. One then solves the upper part of the right-hand side in real space and the lower part in Fourier space [27, p. 294]

and deleted as

$$p_{\text{del}} = \min \left[ 1, \frac{1}{1 + \frac{V \exp(\beta\mu)}{\Lambda^3 N} \exp(\beta(E_{t+1} - E_t))} \right]. \quad (3.14)$$

Here  $E_t$  is the energy at time step  $t$ ,  $V$  the volume,  $N$  the number of particles in the system before the insertion/deletion,  $\Lambda$  the thermal de Broglie wavelength, and  $\mu$  the chemical potential (see eqs. 4.39 to 4.43 in [29]).

### 3.5 Ewald Summation

In a periodic box, there is an infinite number of more and more distant neighbors. In theory, all of them are a part of the potential experienced by a given particle. However, some particles (or mirror images of them) contribute more to the potential than others. At a certain point where the distance is large enough and the sum over all contributions to the potential converges, one can cut off all contributions smaller than a given, acceptably small value. The Coulomb potential, unfortunately, converges extremely slowly and not even in all cases [27]. Therefore, a cutoff presents the choice between very heavy computational costs and/or inaccurate Coulomb potentials, especially in a periodic system. One approach to use, instead of truncation, is a technique called Ewald summation.

Considering only point charges in a cubic of box of volume  $L^3$ , the electrostatic

potential  $\phi$  of the  $i$ th particle at point  $\mathbf{x}_i \in L^3$  can be written as

$$\phi_{\text{point}}(\mathbf{x}_i) = \sum_{j,\mathbf{n}} \frac{q_j}{|\mathbf{x}_i - \mathbf{x}_j + \mathbf{n}L|} \quad (3.15)$$

where we sum over all particles  $j$  and all periodic images  $\mathbf{n}$  of the cubic box with side length  $L$ . The case of  $i = j$  is excluded for  $\mathbf{n} = \mathbf{0}$  as one does not want to include self-interaction (while including the interaction with their mirror images).

In the case of Ewald summation, we now add a cleverly chosen zero for every charge  $q_i$ . We add both a screening charge distribution in the shape of normal distribution, i.e.

$$\rho(\mathbf{x}_i) = -q_i(\alpha/\pi)^{3/2}e^{-\alpha x_i^2} \quad (3.16)$$

as well as a compensating charge distribution of opposite sign. The width of the distribution  $\sqrt{2/\alpha}$  is chosen based on grounds of computational efficiency. We thus get

$$\phi_{\text{point}}(\mathbf{x}_i) = \underbrace{\phi_{\text{point}}(\mathbf{x}_i) - \phi_{\text{Gauss}}(\mathbf{x}_i)}_{\text{Real part}} + \overbrace{\phi_{\text{Gauss}}(\mathbf{x}_i)}^{\text{Fourier part}}. \quad (3.17)$$

This allows us to split the Coulomb interaction into two parts, one quickly converging in real space and the other in Fourier space. As illustrated in the top right corner of Fig. 5, in the real part, we match a point charge  $q_j \delta(\mathbf{x}_i - \mathbf{x}_j)$  with a corresponding oppositely charged Gaussian charge distribution  $\rho(\mathbf{x}_j)$ . Their contribution decreases quickly with increasing distances. At the same time, after converting the other Gaussian to Fourier space, the second term becomes a sum of delta functions which also can be efficiently calculated. We can combine the results of those two calculations and define the  $\mathbf{k}$ -space charge distribution  $\rho(\mathbf{k})$  as

$$\rho(\mathbf{k}) \equiv \sum_{i=1}^N q_i \exp(i\mathbf{k} \cdot \mathbf{x}_i). \quad (3.18)$$

with  $\mathbf{k}$  as the Fourier space coordinate. Then the interaction potential reads as

$$V_{\text{Coul}}(\mathbf{x}_i) = \frac{1}{2L^3} \sum_{\mathbf{k} \neq 0} \sum_{j=1}^N \frac{4\pi q_i q_j}{k^2} e^{-k^2/4\alpha} e^{-i\mathbf{k} \cdot (\mathbf{x}_i - \mathbf{x}_j)} - \sqrt{\frac{\alpha}{\pi}} q_i^2 + \frac{1}{2} \sum_{i \neq j} \frac{q_i q_j (1 - \text{erf}[\sqrt{\alpha} |\mathbf{x}_i - \mathbf{x}_j|])}{|\mathbf{x}_i - \mathbf{x}_j|}. \quad (3.19)$$

The first term is the result of the Fourier sum over all charges. It includes the self-interaction of the particle which we do not want to include (not to be confused with the desired interaction with its own mirror images). To remedy this, we include the second term. This term is constant for systems of a fixed number of particles. The real space contribution is given by the third term where  $\text{erf}$  is the error function. A more detailed analysis can be found in Ref. [27].

If the system is not periodic in one of those dimensions, one would intuitively like to rewrite Eq. (3.15) with  $\mathbf{n}$  only summing over two dimensions. After converting to the three-dimensional Fourier space, however, this leads to a more complicated (and a more computationally expensive) expression than the solution in 3D space. A common workaround is to insert a large vacuum in the non-periodic dimension and then use the original three-dimensional method<sup>4</sup> [31].

### 3.6 Walls

The slit restricts the movement of the particles in the third dimension. In our simulation, we need to do the same.

In the lab, the walls are usually made of 3D structures such as graphite. Implementing a 3D structure of atoms at the bottom and top of our slab would mean that over nine-tenths of the atoms in our simulation would be part of the walls. The first layer represents the by far strongest contribution of the particle-wall interaction. Thus, a somewhat more computationally efficient approach is to implement a wall made up of a single layer wall on either side. In either case, to maintain the desired distance  $h$ , one has to forbid the particles in the wall from moving. In some of our simulations, we follow this approach. For this, we put carbon atoms on a hexagonal grid, where each atom has three neighbors at a distance of 0.142 nm. Yet even with a single layer at the top and bottom of the simulation, carbon atoms represent a majority of atoms in the simulation.

For our slits, we use atomically flat structures yet they still have some structure. Compared to the idealized flat wall, this can lead to slightly different distributions in the out-of-plane dimension as particles can spread out further in “holes” and less so “on top of” carbon atoms. Different walls were shown not to affect the general properties of conductivity [11]. A way to introduce such an idealized wall is the Lennard-Jones 93 potential (LJ93). One can easily integrate over the effect a uniform wall has on a particle. In the case of walls without charge (such as graphene), this can be fully described by the LJ potential [32] and one obtains

$$V_{\text{LJ93}}(r_z) = \frac{2\epsilon}{15} \left[ \left(\frac{\sigma}{x_z}\right)^9 - \left(\frac{\sigma}{x_z}\right)^3 \right]. \quad (3.20)$$

Here,  $x_z$  is our position variable in the out-of-plane dimension. It is 0 at the location of the slit. The other parameters are the regular LJ parameters (of graphene). Instead of calculating the Lennard-Jones interaction of every moving particle with every wall particle, one has to calculate just one value. The effect is a drastic reduction in computation time, roughly scaling with the share of particles allocated to build the wall. In our case, this reduction made simulations five times quicker.

Walls made from different materials have slightly different permittivity but they do not change the conductive properties of the system qualitatively [11].

---

<sup>4</sup>This is also what the LAMMPS slab correction does [30].

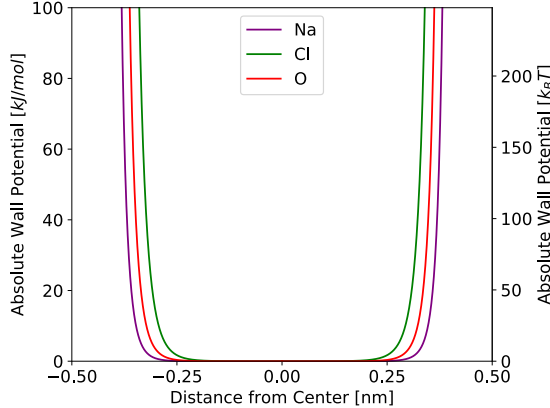


**Figure 6: Wall repulsion experienced by different particles.** We show the Lennard-Jones 93 potential between a graphene-like wall and oxygen, sodium, and chloride.

Both the continuous as well as the atomistic wall are soft rather than hard walls. Even if our walls are situated at a distance of  $h$ , particles do not occupy the full space as they are repelled by the wall before reaching its center. The effective volume which can be occupied is thus reduced by the effective diameter of our wall – in fact, even extending slightly beyond that as shown in Ref. [12]. Following the approach of Ref. [12], we reduce the effective volume of our box by 0.34 nm in calculations involving the volume of the slit.

### 3.7 Potential of Mean Force

In a molecular dynamics simulation, we employ the Coulomb and LJ force fields to determine whether two particles attract or repel each other. However, particles interact not just with one but with all surrounding particles. Particles can also affect each other indirectly by for example blocking the interaction with other particles. To measure a particle's effect on another, we first need to choose a relevant parameter for their interaction. In our case, that is the distance. Then we want to measure the change in the overall free energy as a function of the distance between the two particles. The free energy surface along the distance is then the potential of mean force (PMF).

There are several ways to calculate PMFs. The easiest way is to run a simulation by inserting a single ion pair into the system without any further modifications. Then, one records both the distance between the two particles as well as the change in free energy until we have sampled enough values for all relevant distances. The issue with this approach is that locations are potentially sampled unevenly, in which case it can take a very long time to sample all the interesting distances. In our case, for example, we are interested in the change in free energy right next to the strongly repelling core of the ions.

However, we don't have to rely on statistics and force particles to explore distances more evenly. This can be done by either fixing particle positions in specific locations or by adding an additional force to move the particles towards anchoring locations. We will now look at both approaches in detail in the upcoming two sections.

### Constrained Bias

In the case of constrained bias, we initialize a simulation box for a set of distances  $r$  between the cation and anion. We record all the forces  $\mathbf{F}_k(r)$  the ion  $k$  experiences every few time steps  $\Delta t_{\text{record}}$  and group them by the  $r$ . Then, we project the forces in the direction of the other ion by introducing the unit vector  $\pm \frac{\mathbf{r}_{ij}}{r}$  connecting the two ions. Finally, we take the average of the two forces as well as the time average, so that we obtain the following interaction force

$$F_{\text{PMF}}(r) = \frac{1}{2} \langle (\mathbf{F}_{\text{cation}}(r) - \mathbf{F}_{\text{anion}}(r)) \cdot \frac{\mathbf{r}_{ij}}{r} \rangle. \quad (3.21)$$

The averaging removes forces acting the same way on both particles and intensifies the forces which push the particles in opposite directions, i.e. either towards or apart from each other. As the distance between the two ions is the only thing that changes between different runs,  $F_{\text{PMF}}$  is exactly the rate at which the free energy changes, i.e.  $F_{\text{PMF}} = -\frac{\partial}{\partial r} U$ . Thus, we can now obtain the potential  $U(r)$  by

$$U(r) = - \int_r^{r_\infty} F_{\text{PMF}}(r') dr'. \quad (3.22)$$

If the particles are not rotation invariant, one has to account for different orientations. This is tedious if one keeps positions fixed. Furthermore, one is limited by the number of data points one collects.

### Umbrella Sampling

In Umbrella sampling, the aforementioned issues are tackled. One still has several simulation windows but the positions are not kept fixed anymore. Instead, to each simulation window  $k$ , we add a biasing potential  $\omega_k(r)$ , making states around the reference point  $r_{0,i}$  more energetically favorable. This allows us to explore many different values for our reaction coordinate in a single simulation. From the biased distribution  $p_k^s(r)$  between the ions  $i$  and  $j$ , one can extract the unbiased potential of each window  $U_k$  as shown in [33] yielding

$$U_k(r) = -k_B T \ln p_k^s(r) - \omega_k(r) + C_k. \quad (3.23)$$

From this expression, we have to calculate the overall potential  $U = \sum_k b_k(r)U_k(r)$ , with  $\int_0^{r_\infty} b_k(r) dr = 1$ . Each window has its own constant offset  $C_k$ , which first

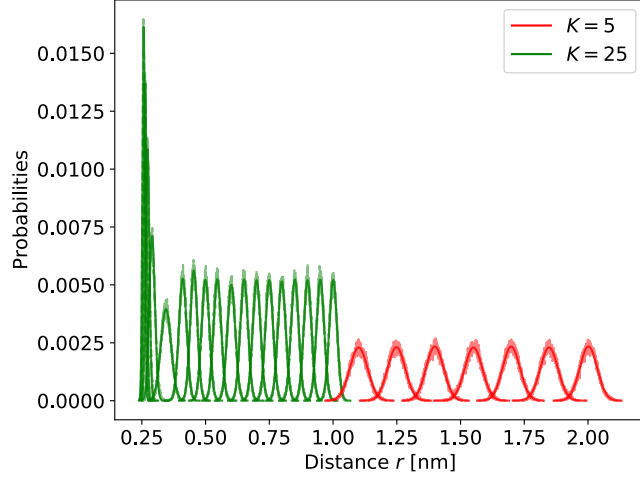


Figure 7: **Biased distribution of NaCl.** Range of biased distributions for a various spring potential  $\omega_k K/2(r - r_{0,k})$ . The spring constant  $K$  is shown in the legend and  $r_{0,k}$  ranges from 0.1 nm to 2 nm. Each individual bell curve was fitted with a Gaussian distribution. The lowest  $\bar{R}^2$  value is 0.98.

needs to be determined to solve this equation right away. There are different approaches to solve this. We will focus on a method called umbrella integration, where we calculate the forces instead of the energy for each location and window. By calculating the derivative of  $U_k$ , we avoid calculating the constant  $C_k$  for each window. Then, the forces are stitched together and integrated to obtain  $U$ . To calculate the forces, we need to first describe how our biased distributions are calculated.

At every measurement, we record the Euclidean distance between the ions. We split the Euclidean distance into discrete intervals of constant width  $\Delta r$  and calculate a histogram for each window. To properly normalize this to a probability distribution, we divide the number of measurements  $N_k^s(r)$  in a bin with its center at distance  $r$  by the volume of the bin  $V_k(r)$  and the total number of measurements of the window  $N_k^{\text{Window}}$  such that

$$p_k^s(r) = \frac{N_k^s(r)}{V_k(r)N_k^{\text{Window}}}. \quad (3.24)$$

For the bulk system, this means we get spherical rings and account for that by dividing the measured frequencies by the difference in volume given by their inner and outer shell. Thus the volume  $V_k(r)$  of the bin with center at  $r$  is given by

$$V_k(r) = 4\pi \int_{r-\Delta r/2}^{r+\Delta r/2} r'^2 dr' = \frac{4\pi}{3} \Delta r \left( r^2 + \left( \frac{\Delta r}{2} \right)^2 \right). \quad (3.25)$$

In the case of our slit system, this is not possible. In the out-of-plane dimension, the slit is a lot smaller than the largest distances considered. To account for that, we do

the following. For distances smaller than  $h/2$ , we use the same method as for the bulk. If the center of the bin is larger than  $h/2$ , however, this method would give us more volume than there is in the slit. Therefore, in the out of plane dimension, the volume does not increase any further, leading to

$$V_k(r) = 4\pi \frac{h}{2} \int_{r-\Delta r/2}^{r+\Delta r/2} r' dr' = 2\pi h r \Delta r. \quad (3.26)$$

We show an example of a range of bias distributions in Fig. 7. Now that we have calculated the biased distributions, we can almost calculate the mean force with

$$\frac{\partial U_k(r)}{\partial r} = -k_B T \frac{\partial \ln p_k^s(r)}{\partial r} - \frac{\partial \omega_k(r)}{\partial r} \quad (3.27)$$

To be able to do this we still need to calculate a derivative of  $p_k^s(r)$ . To achieve this, we approximate  $p_k^s(r)$  up to its second term yielding

$$p_k^s(r) = \frac{1}{\sqrt{2\pi}\sigma_i^s} \exp \left[ -\frac{1}{2} \left( \frac{r - \langle r \rangle_k^s}{\sigma_i^s} \right)^2 \right]. \quad (3.28)$$

This is nothing else than the normal distribution, with the mean  $\langle r \rangle_k^s$  and standard deviation  $\sigma_i^s$  of  $r$  in each window. The assumption of a normal distribution holds as long as the free energy is smooth and each window only covers a small area of the reaction coordinate. However, the quality of this fit should always be checked by calculating a measure for the quality of the fit such as the coefficient of determination  $R^2$ .

To avoid further approximations, the biasing potential should have a derivative that can be calculated analytically. Throughout this work, we choose the harmonic spring potential

$$\omega_k(r) = \frac{K}{2}(r - r_{0,k})^2 \quad (3.29)$$

as our biasing potential, with  $K$  being the spring constant. The choice of  $K$  determines with which force the ions are pulled towards the  $r_{0,k}$ . Thus, it effectively determines the width of the bins and should therefore be chosen as low as possible – without compromising the normal distribution of measurements.

After having specified all of the above, we can now insert this into the derivative of Eq. 3.23. We then obtain

$$\frac{\partial U_k(r)}{\partial r} = -k_B T \frac{r - \langle r \rangle_k^s}{(\sigma_i^s)^2} - K(r - r_{0,k}). \quad (3.30)$$

To obtain the actual force measured at every point, we now need to stitch the results from the different simulations together. For this, we add them together weighted by the overall number of measurements  $N_k^{\text{Window}}$  taken per window  $k$ . This yields the following effective force

$$\frac{\partial U(r)}{\partial r} = \sum_k b_k \frac{\partial U_k}{\partial r}(r) \quad \text{with} \quad b_k(r) = \frac{N_k^{\text{Window}} p_k^s(r)}{\sum_l N_l^{\text{Window}} p_l^s(r)}. \quad (3.31)$$

Now, just like in the case of the constrained bias, we need to integrate along our reaction coordinate to obtain the actual relative free energy which yields

$$U(r) = - \int_r^{r_\infty} \frac{\partial U(r)}{\partial r} dr. \quad (3.32)$$

This is the desired potential of mean force.

## 4 Results and Discussion

In the following, we will present our results and discuss their implications. For each section, we also add a table with a brief summary of the quantitative parameters used so that comparisons between sections are easy as well as their replication.

### 4.1 Attaching a Water Reservoir

GCMC	Values
$L_x = L_y$	2 nm <sup>2</sup>
Slit (Bulk) height: $h$	0.7 nm (2 nm)
Time Step $\Delta t$	1 fs
Time between GCMC Exchanges $\Delta t_{\text{GCMC}}$	0.1 ps
Insertion/Deletion Attempts per GCMC exchange	400
Ion pairs $N_{\text{ions}}$	0 to 5
Chemical Potential $\mu$ of Water Wall	-16 kcal/mol <sup>-1</sup> to -8 kcal/mol <sup>-1</sup> Monolayer graphene

Table 2: List of simulation parameters for the grand canonical simulations

To begin, we wanted to see whether water would flow in or out of our system if connected to a reservoir of water. For this reason, we study how receptive the nanoconfined slit is by attaching a grand canonical simulation. So, we create both a square slit of length  $L_x = L_y = 2$  nm and height  $h = 0.7$  nm as well as a bulk system in a cubic box of length  $L = 2$  nm. We use periodic boundary conditions for the bulk system as well as for the slit in the plane spanned by  $L_x$  and  $L_y$ . In the out-of-plane dimension of the slit, we use two graphene sheets to construct the walls. To initialize either system, we inserted between 0 and 5 NaCl ion pairs as well as 8 water molecules<sup>5</sup>. To make our ions and water molecules move over time, we use the Velocity Verlet algorithm and fix their temperature by applying a Nosé-Hoover Thermostat. We treat the water grand canonically by fixing its chemical potential  $\mu$  in the reservoir and thus allow for the insertion/deletion of water molecules at an arbitrary position in our box. Every 100 fs, we try 400 GCMC insertions and deletions with  $\mu$  between -16 kcal/mol and -8 kcal/mol. We ran those for a total of 100 ps. All relevant quantitative information to replicate this experiment, we summarized in Tab. 2.

In Fig. 8(a), we show as an example how the number of water molecules changes over time for a given number of ions and several  $\mu$ . Starting from the same number of water molecules, they quickly equilibrate towards the energetically most favorable configuration and begin to stabilize around a value. For the other plots in Fig. 8, we take the average of the last 10 ps of the simulation.

---

<sup>5</sup>In the legends of Fig. 8, we convert the number of ions into ion concentrations using Eq. (2.4).

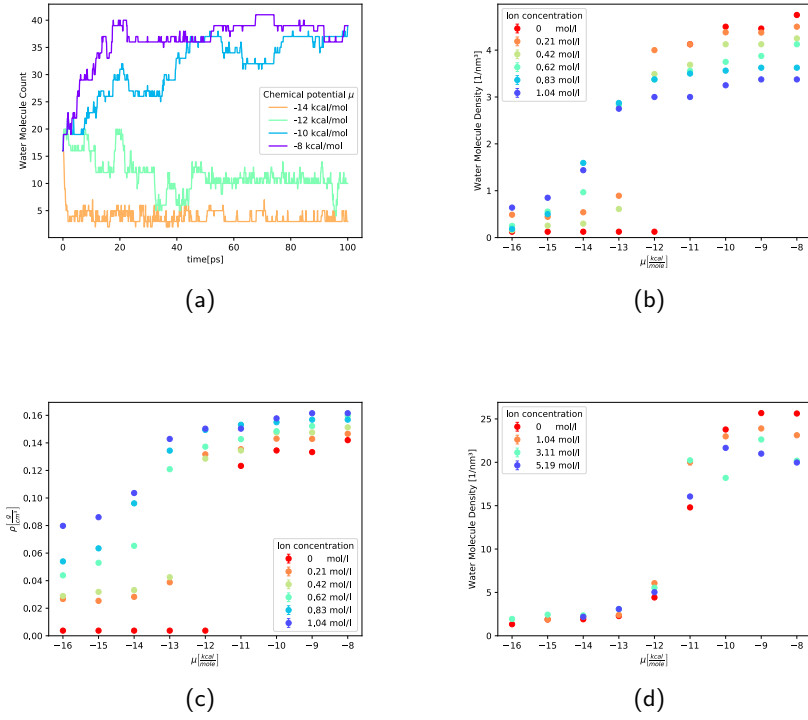


**Figure 8: GCMC of slit and bulk.** Using GCMC, water molecules are inserted every 0.1 ps. More general details are in Tab. 2. (a) Water molecules plotted over time for a single ion pair (or molarity of 0.21 mol/l) in the bulk system of size of  $2 \times 2 \times 2 \text{ nm}^3$ . (b) Water molecule number densities are displayed for a range of chemical potentials and ion concentrations in the same system. (c) Using the same data, we show the mass density of the system. (d) Water molecule number densities are shown for a range of chemical potentials and ion concentrations in a slit of size  $2 \times 2 \times 0.67 \text{ nm}^3$ . The error bars of all plots are based on single simulations and have time correlations.

The error bars are based on a single simulation and have thus a temporal correlation. This means that a small error does not necessarily imply that it is close to the ensemble average. If there is a larger error bar, however, this is an indication that this value is less certain.

In Fig. 8(b), we plot the water molecule density as a function of the chemical potential  $\mu$  for the bulk. It displays a monotonous relationship between the number of water molecules and the corresponding  $\mu$ . Without the presence of other atoms, there is just a single water molecule for chemical potentials below  $-11 \text{ kcal/mol}$ . Then, a difference in  $\mu$  doesn't lead to different behavior. If there are salt ions present, water flows into the bulk at lower chemical potentials as well and the more ions there are, the more water flows into the bulk system. For higher chemical potentials, this is not the case. More accurately, this occurs once a certain number of water molecules is surpassed. The space in the simulation box gets scarcer and thus the insertion of another water molecule becomes harder. In Fig. 8(c), we show the mass density of the same data as displayed in Fig. 8(b). Here we see that indeed the density scales monotonously with the number of ions at all chemical potentials in the bulk.

Comparing the curves for the bulk case with the slit Fig. 8(d), we notice two main differences. The first to note is the higher density of water molecules. At any chemical potential and number of ions, there are more water molecules in the slit than in the bulk. The second is that in the slit, higher numbers of ions do not attract more water at a low chemical potential. Yet at high chemical potentials, we see a similar pattern as in the case of the bulk.

Of special interest is the behavior of water at ambient conditions. At room temperature, we know that water has a density of around  $1 \text{ g/cm}^3$ . This corresponds to a  $\mu$  of  $-11 \text{ kcal/mol}$  for the bulk case. From the Maxwell relations, we know the following holds for an incompressible fluid and constant temperature

$$\Delta p = -\rho \Delta \mu. \quad (4.1)$$

Here,  $\Delta p$  is the change in pressure and  $\rho$  the number density of the particle species. This in turn means that for a given  $\mu$  the ratio of the number densities is equivalent to the ratio of the change in pressure as in  $\frac{\Delta \rho_{\text{slit}}}{\Delta p_{\text{bulk}}} = \frac{\rho_{\text{slit}}}{\rho_{\text{bulk}}}$ . This means the slit experiences a higher change in pressure. This difference is consistent for all values of  $\mu$  from a vacuum onwards. To compare the levels of overall pressure in bulk and slit, this implies that the pressure in a nanoslit is a lot higher than in the bulk. We will have another look at the pressure in the next subsection.

We need to note that the molarity of the simulated solution is extremely high. In the slit, the molarity of the single ion pair is higher than that of seawater (at around  $0.6 \text{ mol/l}$  [34]). This means to show that any effect of this system is significantly more intensive than one would expect in most real-world settings.

Unfortunately, GCMC is a very slow simulation technique and its implementation in LAMMPS did not allow for speed-up techniques such as using multiple processing

units for the same simulation. we chose to move ahead and study larger systems in the  $NVT$  ensemble.

## 4.2 Diffusion

For the next part, we want to investigate whether ions observe Brownian motion under nanoconfinement. For this, we focus on the most common – and most studied – of the salts at hand, sodium chloride (NaCl). We study ion concentrations between 0.03 mol/l and 2 mol/l (corresponding to inserting between 1 and 80 ion pairs). We insert the ions randomly and let the system equilibrate. The slit has the same size and the same continuous LJ93 walls and also the attached thermostat, time integration, duration, and time step remain the same as before. In this simulation, we use water molecule density of  $21.8 \text{ nm}^{-2}$ . All parameters relevant to recreating the simulation are also summarized in Tab. 3.

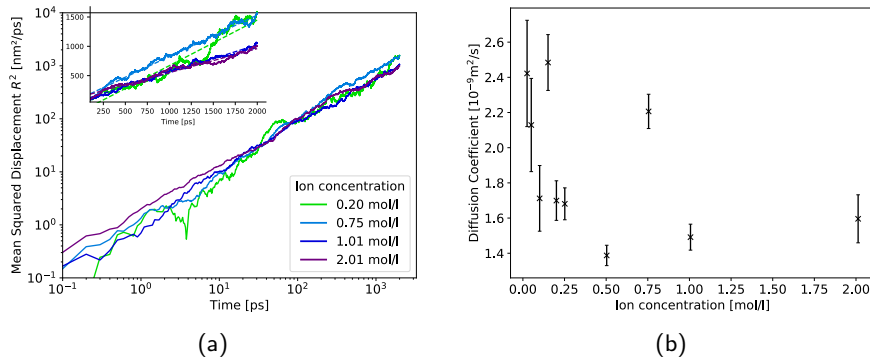
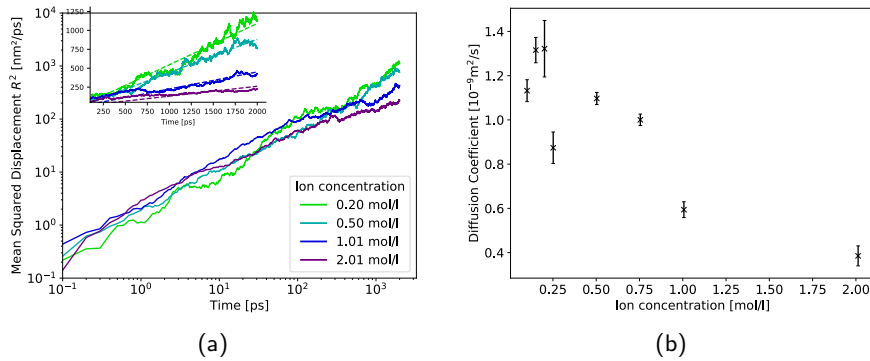


Figure 9: **Mean squared distance and diffusion coefficient of NaCl.** We perform MD simulations on NaCl in system as described in Tab. 3 with no electric field. (a) We show the mean squared distance for a range of ion concentrations. The cutout in the top right corner represents a zoomed-in version with linear fits in dashed lines. (b) The diffusion coefficient is calculated with Eq. (2.8) in 2 dimensions. The mean and standard error of the mean are calculated by discarding the first 0.5 ns and splitting the rest in windows of 0.25 ns.

We show the mean squared displacement  $R^2(t)$  of various ions in the plane in Fig. 9(a). For this, we do not consider the out-of-plane dimension as particles cannot travel far in that dimension. We use linear fits to confirm that we are indeed in a system of diffusion which we show in the top right corner of Fig. 8(a). For lower concentrations, we see some deviations from the linear trajectory. At a concentration of 0.20 mol/l (the lowest shown), there are only 8 ion pairs in the system. So we can assume that this is simply a statistical fluctuation. We see however that not all ion concentrations have the same slope.

To quantify the behavior at long distances, we calculate the two-dimensional dif-

fusion coefficient  $D$ . We split our simulation into windows of 0.25 ns, calculate the diffusion by Eq. (2.8) and show the average and standard error of the mean in Fig. 9(b). What we find is that our error bars are rather small. Yet we obtain very different outcomes for similar ion concentrations. From this, we conclude that the ergodic hypothesis does not hold and the time averages do not give a good picture of the ensemble average. This means that single runs are not a good guide to study the general diffusion properties and that amount of pairs/clusters has a strong influence on the diffusive properties of the system.



**Figure 10: Mean squared distance and diffusion coefficient of generic ion of valence  $Z = 2$ .** We perform MD simulations on a generic ion with valence  $Z = 2$  and the LJ parameters of NaCl in the system as described in Tab. 3 with no electric field. (a) We show the mean squared distance for a range of ion concentrations. (b) The diffusion coefficient is calculated with Eq. (2.8) in 2 dimensions. The mean and standard error of the mean are calculated by discarding the first 0.5 ns and splitting the rest in windows of 0.25 ns.

To study the effect of charge on the diffusion, we also look at the  $R^2(t)$  of a divalent generic ion and show their  $R^2(t)$  in Fig. 10(a). Here, we see the same linear behavior as in the monovalent case. For short time scales, ions move faster in systems of higher concentrations. This reverses at time scales of around 10-100 ps. After around 100 ps, we see that ions move faster at lower concentrations.

The behavior at larger time scales dominates of course when calculating diffusion coefficients  $D$  which we show for a range of concentrations in Fig. 10(b). Unlike before, we observe a clear decreasing relation for  $D$  with respect to the ion concentration. Also, the diffusion coefficient for the case of the divalent case is roughly half that of the monovalent case. By design, the only difference lies in the valence of the ions. Therefore, the ions' increased attractiveness leads to lower mobility. Combined with the fact that highly concentrated ions move more quickly at an earlier stage, we assume the following occurs. Ions that are in close vicinity to an oppositely charged ion move towards this ion at high speed. Once they find that

ion, they move more slowly. At high concentrations, many ions are nearby leading to a lot of movement early on – and subsequently to a slowdown.

### 4.3 Constant Electric Field

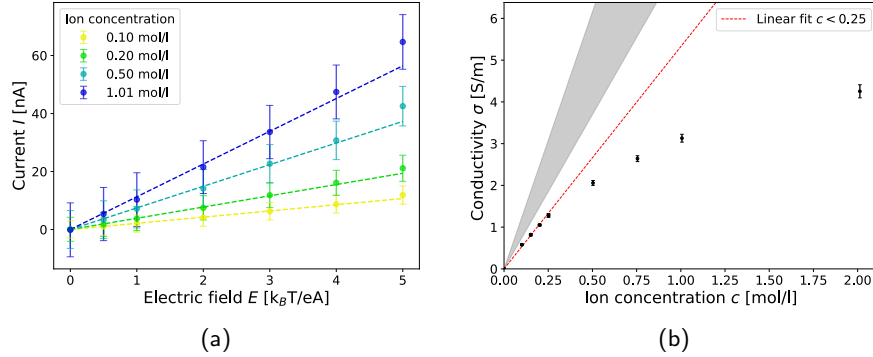
MD: E-field & Diffusion	Values
$L_x \times L_y$	$10 \times 10 \text{ nm}^2$
Slit height $h$	1 nm
Time step $\Delta t$	1 fs
Run time	1 ns
Ion pairs $N_{\text{ions}}$	5 to 100
Electric Field $E$	$0 \text{ k}_B T/\text{e}\text{\AA}$ to $5 \text{ k}_B T/\text{e}\text{\AA}$
Water Molecule Density $\rho$	$21.8 \text{ nm}^{-2}$
Wall	LJ93 based on Carbon

Table 3: List of simulation parameters in current, conductivity and diffusion experiments

Next, we turn our attention to the behavior of ions in electric fields. Besides adding an electric field, we use the exact same system as in the previous section. The dimensions of the slit, the synthetic LJ93 walls as well as the attached thermostat, time integration, duration, and time step remain the same as before. Now, of course, we add an electric field which we varied between 0 and  $5 \text{ k}_B T/\text{e}\text{\AA}$ . As before, we will first look at NaCl and then compare its behavior with the divalent case.

As we see in Fig. 11(a), for the case of sodium chloride, we observe a, within the error bars, linear relationship between electric fields and electric currents. Only for the strongest electric field,  $5 \text{ k}_B T/\text{e}\text{\AA}$ , does the measured value lie above the fit line, yet still at around the edge of our error bar. Both the linear correlation overall as well as the outlier for the largest electric field, we find a wide range of ion concentrations beyond the ones shown in Fig. 11(a). We make use of this to calculate the conductivity  $\sigma = \frac{1}{A} \frac{I}{E}$ . This means the behavior of sodium chloride is primarily described by the Ohmic relation.

We use the slope of the linear fit in Fig. 11(a) to calculate  $\frac{I}{E}$  and use Eq. (2.6) so we only need to rescale our fits with the area through which the current passes. We then obtain the conductivity and plot them as a function of concentration as shown in Fig. 11(b). For low concentrations, we see a linear relationship between conductivity and concentration. This is what we would expect as the electric field, in the dilute limit, scales with the number of ions in the system. For concentrations larger 0.5 mol/l, the conductivity does not scale with ion concentration as before. This means that the addition of further particles does not lead to a corresponding increase in conductivity. In turn, we can deduce from this that there are density/concentration-dependent effects on the conductivity. We explain this with an increase in clustering. The overall chance to find another particle in close vicinity scales with the number of particles already in the system. If we compare



**Figure 11: Applying constant electric fields to confined NaCl.** (a) Electric currents for different ion concentrations. Dashed lines are linear fits. The error bars are calculated by grouping calculation in chunks of 0.25 ns. Simulation ran for 2 ns. (b) Conductivity calculated using the slope of the linear fit as shown in (a) together with Eq. (2.6). In grey, we present the conductivity as expected by the upper and lower bound of diffusion coefficients shown in Fig. 9 together with the Nernst-Einstein equation (Eq. (2.9)).

conductivities measured in this section with the ones that we would expect based on the Nernst-Einstein equation (Eq. (2.9)), we see that even at the lowest concentrations, the conductivity is below the expectation. This underestimation could be explained that even at these rather dilute concentrations some pairing occurs. Because ions that pair up still move, contributing to the mean squared displacement. Yet, they do not contribute to the current anymore. However, one should also take note that we are in a regime of very few actual ions (a concentration of 0.05 mol/l corresponds to just two ion pairs).

If we now double the charge of the ions, the picture changes drastically. For divalent ions, we find that there is a nonlinear correlation between electric currents and electric fields. For lower electric currents, we see a lower conductivity and for larger electric fields, we observe a higher conductivity. This implies that our electric field pulls ions towards each other in the weaker electric fields and apart in the stronger electric fields.

Eq. (2.5) states that the electric current scales with the charge of ions moving at unchanging speed. At the same time, the force ions experience in an electric field also scales with their charge. In total, the expected current in the divalent case ought to be four times as large compared with the monovalent case. Yet the overall current is lower in the divalent case compared to the monovalent case. Instead, we observe a lot more clustering occurring, reducing the desire of the ions to move along the electric current. On top of this, considering the error bars, one can hardly

differentiate the current for concentrations of 0.2 mol/l and 2 mol/l even though the current ought to scale linearly with the concentration – without correlation of the ions, that is. As previously discussed, when ions form pairs, their effective contribution to the current becomes zero. Therefore, only free ions and at most one free ion per cluster (group of three or more particles) contribute to the current. From this, we conclude that the number of free ions is reduced at higher electric fields.

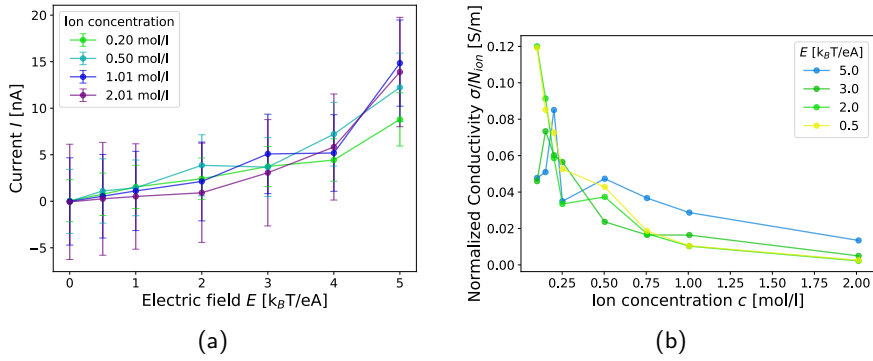


Figure 12: **Applying constant electric fields to confined NaCl.** (a) Electric currents for different ion concentrations. The error bars are calculated by grouping calculation in chunks of 0.25 ns. Simulation ran for 2 ns. (b) Electric Conductivity is divided by the number of ions  $N_{ion}$  and the electric field applied.

To study the effect on the conductivity, we cannot simply calculate a linear fit to obtain something representative of a given ion concentration. For this reason, we define and calculate a notion of normalized conductivity  $\hat{\sigma}$ . We obtain  $\hat{\sigma}$ , by dividing over both the electric field applied and the number of ion pairs  $N_{pairs}$  present in the given run, yielding

$$\hat{\sigma} = \frac{I}{EN_{pairs}} \quad (4.2)$$

In Fig. 12(b), we plot this for several electric fields in relation to the ion concentration. In the case that our ions do not depend on the concentration, we thus expect a straight line. If the strength of the electric field doesn't influence behavior, we expect lines to overlap. What we see is that neither of those expectations fully holds. For electric fields up to  $2 k_B T/e\text{\AA}$ , we see a very negative correlation with the ion concentration while the electric field has little influence. For larger electric fields, we see less of a correlation with concentration. This means, that for low concentrations, we see a relatively low normalized conductivity and for higher concentrations, we see a higher normalized conductivity. This implies at low concentrations, we see a higher amount of clustering for stronger electric fields than for weaker ones. Yet at low concentrations and strong electric fields, the normalized conductivity is higher than for any electric field at higher concentrations. With stronger electric

fields, ions travel further more quickly. This means the chance of encountering an oppositely charged ion increases. At higher concentrations, we see higher normalized conductivities for stronger electric fields. This would imply that at sufficient concentrations, finding another ion is not constraining anymore. Instead, the force of the electric field pushing oppositely charged ions in different directions leads pairs that have formed to dissociate earlier than in lower electric fields. To compare this chart with the one for sodium chloride, we refer to Fig. 25 in the appendix.

One caveat of this analysis is the question of how physical it is to apply electric fields of this magnitude. Consistent with the literature, we chose to look at electric fields up to  $5k_B T/e\text{\AA}$ . For a system with  $L_y = 10 \text{ nm}$ , this translates to a voltage of  $12.84 \text{ V}$ . This is roughly ten times the voltage required for hydrolysis in a bulk system. For a constant electric field  $E$ , the voltage  $V$  scales as  $V = L_x E$  which means that in larger systems, such as that of [11], hydrolysis sets in at even lower  $E$ . Future research should look at the hydrolysis properties of water under nanoconfinement. If they were comparable to those in the bulk, the covalent bonds of the water molecules would be broken. Consequently, the results of this study could not be physical. If that were the case, future research should look at whether non-Ohmic behavior can be found at lower electric fields as well.

Another caveat is that we found this non-Ohmic behavior for a generic salt rather than a physical one. In the next section, we will, among other things, look at how generalizable these results are.

#### 4.4 Potential of Mean Force

Parameters	MD: PMF
$L_x = L_y$ ; Slit (Bulk)	$10 \text{ nm}^2$ ( $5 \text{ nm}^2$ )
Slit (Bulk) height: $h$	$1 \text{ nm}$ ( $5 \text{ nm}$ )
Time step $\Delta t$	$1 \text{ fs}$
Run time	$1 \text{ ns}^6$
Electric Field $E$	0
Water Molecules $N_{\text{Water}}$	2320
Wall	LJ93 based on Carbon

Table 4: List of simulation parameters in PMF simulations

After having observed static currents, we wanted to investigate such behaviors with time-varying currents. This presented a problem. The molecular dynamics simulations (MD) were simulating our system in the order of nanoseconds per day. As discussed in the literature, the memristive effect was observed at frequencies ranging from kHz to MHz, which require simulation times outside the scope of MD. Previous works in the literature had used generic salts in Brownian dynamics simulations relying on the Q2D potential (as described in Eq. (2.12)). This raised the question of how well the Q2D potential describes the effective interaction between ions under nanoconfinement. In this section, we want to determine effective ion-ion

potentials in a nanoslit as well as in the 3D bulk.

For the most part, we use the same slit as before and insert water molecules at a density of  $23.2 \text{ nm}^{-2}$ . However, we also look at the case of one and three layers of water as well as the 3D bulk system. The slits have the same area and slit heights of 0.7 nm and 1.3 nm, respectively whereas the bulk is made of a cubic box with sidelength  $L = 5 \text{ nm}$ . Then we insert one pair of ions and kept it at a fixed distance or in a small range of distances. We achieve this by not allowing any movement in the constrained bias (CB) case and by attaching a harmonic spring potential between the two ions in the case of umbrella integration (UI), respectively. The exact technique is detailed in the methods section. Except for  $\text{CaCl}_2$ , the PMF simulations are run for 1 ns with a Nosé-Hoover thermostat at 298 K. Every 20 fs, the forces and positions of the studied ions are recorded.

Lastly, our box is not infinitely large, requiring us to choose a finite  $r_\infty$  for Eqs. (3.22, 3.32). We should choose  $r_\infty$  to be at a sufficiently large distance such that  $F_{\text{PMF}}(r_\infty) \approx 0$ . In the case of the bulk, at a distance of 2 nm and unit charges, the Coulomb potential differs by less than 1 kJ/mol to its value at infinity. In the case of a two-layer water slit, the Q2D potential differs by around 10 kJ/mol at a distance of 2 nm and needs a distance of more than 47 nm to fall below the threshold of 1 kJ/mol. It was not feasible to build a system with a size of around 100 nm in box length. As a consequence, we can only construct a partial but not a full PMF from our simulations, assuming that the Q2D is correct. Later, we will then show our best estimate of the effective interaction potential of the ions. To ensure the correctness of those PMFs, we first need to confirm whether the data that we measure is correct.

Both for CB and UI, we take the integral from the distance  $r$  to  $r_\infty$  to calculate the PMF. Therefore, the PMF will always be 0 at  $r_\infty$ . Accordingly, the PMF that we measure is shifted compared to the true effective interaction. To make a sensible comparison between Q2D and the PMFs, we shift the analytic potential to be 0 at  $r_\infty$  as well. As the Q2D interacts at long distances, we also have to account for the effect of periodic images. The first periodic image of the charge has a strong influence, to compensate for this we define an adjusted Q2D potential as

$$\tilde{V}_{Q2D}(r) = V_{Q2D}(r) - V_{Q2D}(L_y - r). \quad (4.3)$$

Now we compute the PMF of NaCl in a slit with height  $h = 1 \text{ nm}$  and plot its CB, UI and the corresponding adjusted Q2D for a distance of up to 2 nm in Fig. 13(a). For both CB and UI, the PMF increases almost monotonously at distances beyond 1 nm. As discussed before, for large distances our distributions approach (since we defined it to be an integral with a finite distance upper boundary, compare with the integrals in Eqs. 3.22 and 3.32). For distances smaller than 0.25 nm, we see that the potential is highly positive and decreasing rapidly. At a distance of 0.25 nm (0.20 nm), the LJ potential of  $\text{Na}^+$  and  $\text{Cl}^-$  evaluates to 13.6 kJ/mol (226.7 kJ/mol), showing that this rise is a consequence of LJ repulsion.

In between, however, both CB and UI show three discernible troughs and peaks

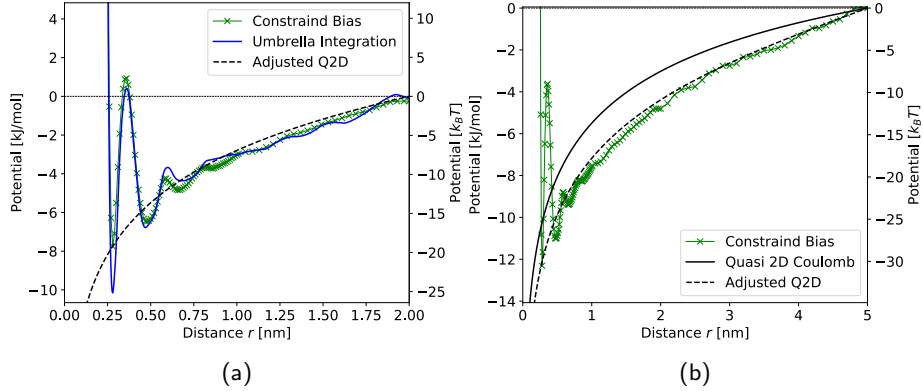


Figure 13: **Validating PMFs.** (a) Calculating the potential of mean forces using the constrained bias (CB) and umbrella integration technique (UI) with a cutoff at 2 nm and comparing with  $\tilde{V}_{Q2D}(r)$ . (b) Comparing CB to both  $\tilde{V}_{Q2D}(r)$  and  $V_{Q2D}(r)$  for distances of up 5 nm.

which differ from the behavior the Q2D potential would let us expect. We see that the global minimum lies at the closest trough and is followed by the largest peak. The potential differences between subsequent peaks and troughs become smaller. The difference between the subsequent peaks and troughs is constant and persistent throughout different PMFs for different salts and systems. The only thing consistent is the existence of water molecules in all these simulations which is why we identify those as the effect of water. As discussed in the theory section, water molecules attach to ions.

We calculated CB and UI from different data using different methods. Yet overall we can state that they are in good alignment as all the characteristic features such as peaks and dips are in the same locations and they have the same slope towards large distances.

At the first trough, we spot the biggest difference which is a lot deeper in the UI case than in the CB case. In both, however, it is significantly deeper than the second trough. The constrained bias case was limited to a single data point per simulation. With Umbrella Integration, one can sample more locations and thus also come closer to the true minima and maxima of the distribution. This is especially helpful in places where forces change quickly with respect to the distance. On the other hand, CB samples a lot more values per location. So in areas with low rates of change, such as for distances beyond 1 nm, it includes less noise.

The additional accuracy close to quickly changing parts of the function is helpful. Also, it restricts the movement of the particles less and thus allows them to interact with the system more “naturally”. The ions can move to their preferred position in the slit (particularly in the out-of-plane dimension) and, in the case of anisotropic

particles, also their preferred orientation. This is why we use Umbrella Integration as our main method. As described in the methods section, one needs to make sure that the underlying assumptions are fulfilled, specifically that the biased distributions follow a Gaussian distribution and that sufficient data was sampled for every bin.

Seeing that our two fairly different methods show the same result gives us confidence that we capture the physics of our system. We now compare the adjusted Q2D potential with the UI and CB. For distances of more than 1 nm, we find that we are in very good alignment. In the case of the Q2D potential, as in the 3D Coulomb potential, the solvent is assumed to be continuous (as is the case for water at a macroscopic scale) and only represented by its relative permittivity. Unsurprisingly, the effects of the water molecules are not represented in the data. However, the Q2D potential approximates the behavior of sodium chloride in the slit very well besides the effect of water (and the LJ repulsion).

Next, we show the difference between  $\tilde{V}_{Q2D}(r)$  and  $V_{Q2D}(r)$  and how they match our CB potential for distances up to 5 nm in Fig. 13(b). We see that the adjusted Q2D matches the CB PMF very well at longer distances as well. The visible difference between the slopes of  $\tilde{V}_{Q2D}(r)$  and  $V_{Q2D}(r)$  shows that the effect of the first mirror image is significant throughout the box. For a more accurate picture of the PMF, the box should have been larger.

Furthermore, in all the experiments on diffusion and ionic currents, each ion experienced the forces of all ions in the box and even their mirror image. When an electric field is applied, ions with an opposite charge move in opposite directions. In a periodic box, ions moving in opposite directions have a higher chance to come close to each other. As we saw above, the interaction between ions is a lot stronger than in the bulk. Therefore, encountering oppositely charged ions could, even if no pairs are formed, lead to a slow down and, thus, a lower current.

### The Effect of Ion Size

To study the effect of size, we consider a different ion of the same valence, lithium chloride (LiCl). The differences between lithium and sodium in an MD simulation lie solely in their respective LJ parameters. Furthermore, we add a second force field for NaCl as given by the Amber force field. All LJ parameters are listed in Tab. 1. We show the measured PMFs in Fig. 14. There is a highly positive, rapidly decreasing potential at very short distances. We observe that the peaks and troughs have the same distance as before. As the LJ diameter for  $\text{Li}^+$  is smaller than for  $\text{Na}^+$ , ions can come closer and thus experience a higher Coulomb force.

If we now take a look at the other set of LJ parameters for NaCl, based on the Amber force field, we find that the first two peaks and troughs are in the same locations. The global minimum is deeper than for either the other NaCl force field or LiCl. The depth of the well (i.e. comparing the minimum with the subsequent local maximum) is the same for NaCl (Amber) and LiCl. Once an ion pair has been found, both have the same potential barrier which needs to be surpassed. From

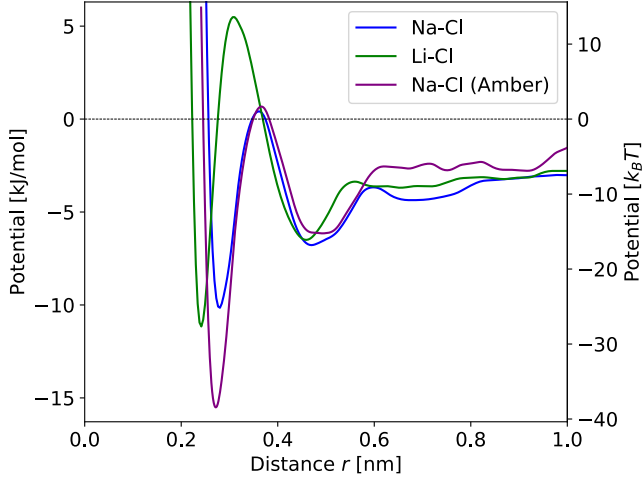


**Figure 14: PMFs of LiCl in the bulk and slit.** The slit is of dimension  $10 \times 10 \times 1 \text{ nm}^3$  and has a water molecule number density of  $23.2 \text{ nm}^{-3}$  whereas the bulk system is of size  $5 \times 5 \times 5 \text{ nm}^3$  and has a mass density of  $997 \text{ kg/m}^3$ .

a distance of  $0.4 \text{ nm}$  onwards, the differences between the three become small. Therefore, the specific parameters play a lesser role at larger distances and are not essential for a phenomenological description of ions that reside in such regimes. For close distances, however, we see that the choice of the force field can influence the quantitative part of our result. From another angle, the difference between using a lithium ion or a sodium ion seems to be fairly limited.

### Comparison of Geometry

Next, we want to compare the behavior of NaCl for different geometries. So far, we looked at a  $1 \text{ nm}$  slit, corresponding to two layers of water. Now, we will add a one and three-layer slit as well which corresponds to slits of widths of  $0.7 \text{ nm}$  and  $1.3 \text{ nm}$ . Based on results in Ref. [7], we choose water molecule densities  $11.5 \text{ nm}^{-2}$  and  $31 \text{ nm}^{-2}$ , respectively. On top of that, we implement a bulk system with a box of  $L = 5 \text{ nm}$  filled with water at the room temperature density of  $997 \text{ kg/m}^3$ , representing the case of an infinitely wide slit. We can calculate the PMF only at shorter distances, due to computational constraints. This box, with a total of 4167 water molecules already contains twice as many water molecules as our regular two-layer slit. However, as we saw in the discussion above the effect of periodic images on the ions is a lot stronger in the slit. To show the true differences between the different slits and the bulk, we have to adjust the measured PMFs because otherwise, the comparisons would be misleading. For long distances, the adjusted Q2D potential matches the measured PMFs very well and we use the Q2D potential to reduce the effects of our box's finite size. To be more precise, we apply a constant shift to account for the fact that the upper limit of our integration  $r_\infty$  is very much

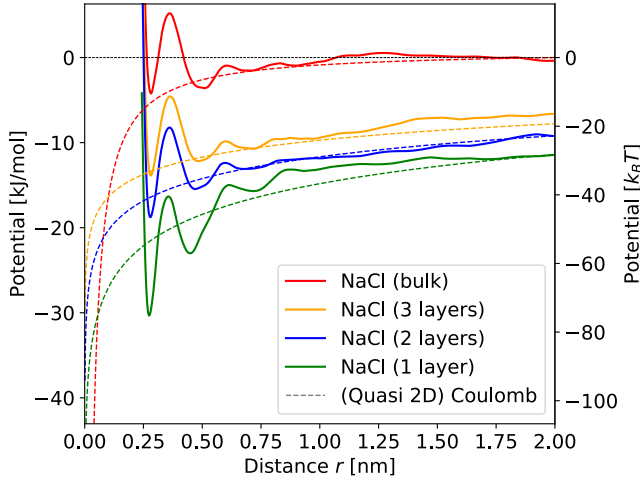


**Figure 15: Comparing the PMFs of NaCl for different geometries.** Using umbrella integration, we compare the PMFs of a single pair of  $\text{Na}^+$  and  $\text{Cl}^-$  for one, two and three water layers (corresponding to a slit height  $h = 0.7 \text{ nm}$ ,  $1.0 \text{ nm}$  and  $1.3 \text{ nm}$ , respectively) as well as the regular volume/bulk case with the corresponding Q2D potential (Eq. (2.12) (or the Coulomb potential Eq. (2.2)) in the bulk case). The measured potentials are shifted as described in Eq. (4.4).

finite, and to reduce the effect of the periodic box we counter the contribution of the first periodic image yielding an adjusted  $\tilde{U}(r)$

$$\tilde{U}(r) = U(r) + V_{Q2D}(r_\infty) - V_{Q2D}(L_y - r). \quad (4.4)$$

When looking at Fig. 15, we see that the overall behavior, i.e diverging for small distances, followed by oscillations and eventually approaching 0, is observed for all four systems. The extrema also lie at the same distances. This is not surprising as neither the shape of the ions nor that of water has changed. Overall, we see that the thinner the slit, the more negative the potential. For the single-layer case, the first minimum is a lot deeper than the second. The wider the slit, the smaller the difference between the two, and in the bulk, the first minimum is at about the same energy level as the second minimum. Also, we see that in their structure the three-layer case resembles the infinite layer case more than the single-layer case and the global minimum lies halfway between the two. Just like in the case of two-dimensional crystals, we see that most of the effect is restricted to the thinnest cases.

Furthermore, there is an increase in the water-induced oscillation for thinner slits. We presume that the extra force comes from the water molecules which cannot move as they want to due to restrictions in their movement imposed by a combination of the ions that we study and the geometry of the slit. In a single layer, water

molecules lie in the same plane as the ion and thus cannot move “through” its x-y location and instead have to move around it. In the bulk case, they can also change their position in the z-component and thus move around it easily. For a slit of a few layers of water the water molecule experiences restrictions, stronger restrictions as some paths might be blocked by the geometry while others are not.

### Univalent Electrolyte

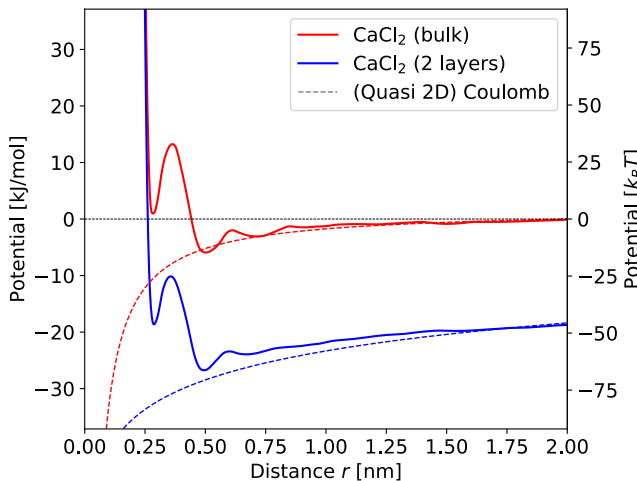


**Figure 16: Comparing the PMFs of bulk and slit for  $\text{CaCl}_2$ .** The slit is of dimension  $10 \times 10 \times 1 \text{ nm}^3$  and has a water molecule number density of  $23.2 \text{ nm}^{-3}$  whereas the bulk system is of size  $5 \times 5 \times 5 \text{ nm}^3$  and water is inserted corresponding to a mass density of  $997 \text{ kg/m}^3$ . The PMFs were calculated with Umbrella Integration and then transformed according to Eq. (4.3). The the Q2D potential as described in Eq. (2.12) and the Coulomb potential as in Eq. (2.2).

So far, we have only considered a single anion and a single cation. In the previous section, one ion was constituted by several differently charged atoms yet they were still moving as one unit. Calcium chloride ( $\text{CaCl}_2$ ) is different as it is a salt consisting of three ions. We are interested in the interaction between  $\text{Ca}^{2+}$  and one  $\text{Cl}^-$  ion. Yet, to have a charge-neutral system, we still inserted the second  $\text{Cl}^-$  ion into the system. It was placed in the vicinity of the two fixed/coupled ions but then left to move freely within the box. To reduce the effect of fluctuations arising due to the third, freely moving ion, we run the simulation for at least 5 ns. We kept track of its position and found that it was never closer to either of the studied ions than they were to each other.

In Fig. 16, we see that  $\text{CaCl}_2$  shares many things with the previously shown PMFs. Again, the subsequent peaks and troughs differ by the same constant distance. There is something different, however. The first minimum of the PMF has a first minimum, followed by a highly positive peak. Only then does the function descend

to the global minimum. This implies that the direct connection is less attractive than the case with a water molecule in between them. From this, we can deduce that  $\text{CaCl}_2$  will not crystallize. However, for dynamic processes such as that of a memristor, it could be suitable.

### Divalent ions

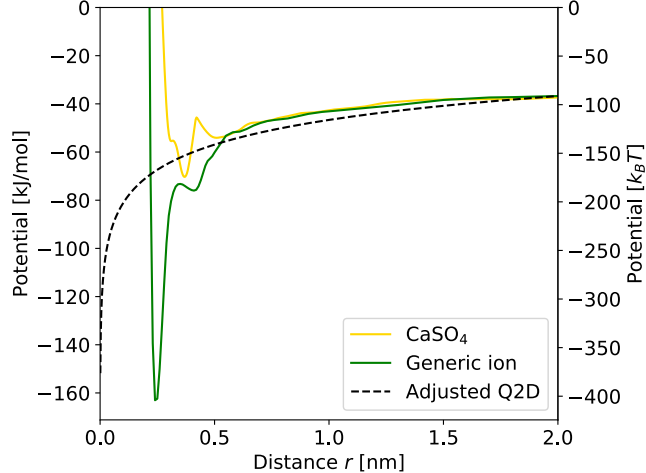


Figure 17: **Comparing PMFs of  $Z = 2$  ions.** Potential of mean force at different distances for  $\text{CaSO}_4$  and  $\text{NaCl}(Z = 2)$  using UI in a slit of dimension  $10 \times 10 \times 1 \text{ nm}^3$ . We compare the PMFs with the adjusted Q2D potential as shown in Eq. (4.3).

As we saw in the previous section, there were some differences between the PMFs of  $\text{NaCl}$  and  $\text{LiCl}$ . We also looked at divalent ions in the sections on diffusion and constant electric fields. To see how applicable the results of our generic ion are, we compare the PMFs of calcium sulfate  $\text{CaSO}_4$  and the generic divalent ion. We plot their PMFs in Fig. 17 together with the Q2D adjusted with the first mirror image. For distances wider than  $0.8 \text{ nm}$ , we see a very good agreement between the two PMFs. The adjusted Q2D tracks them fairly well at those distances. The charge is significantly stronger in this case. Therefore, we assume that an even better match could be achieved if further periodic images were included in the adjustment. At closer distances, we see oscillations due to the water molecules again. As stated in the case of  $Z = 1$ , the Q2D does not capture this effect. Interestingly, the oscillations for both  $Z = 2$  ions are stronger than for  $Z = 1$  ions.

When comparing the two  $Z = 2$  ions with each other, the first thing to note is the difference in the global maximum – both in distance and depth. The global maximum of the generic ion is a lot deeper and at a shorter distance. Shifted by the adjusted Q2D, it is in fact about twice as close and twice as deep. The difference in distance is easily explained by the size of  $\text{CaSO}_4$  which is a lot larger than  $\text{NaCl}$ . This

means that the LJ potential separates the two ions a lot earlier. The doubling of the PMF over a halving of the distance would be in line  $r^{-1}$  with the vacuum Coulomb potential. This would make sense since both minima represent points of closest distance, which means there are no water molecules in the way and the dominant force would come from the electrostatic potential. Given the uncertainty about the shift and the extra correction terms required, this is merely a guess.

For the generic sodium chloride, the peaks and troughs are the same constant distance apart that we saw for the ions with  $Z = 1$ . Compared to NaCl the peaks are all at slightly closer distances. The stronger charge allows the particles to move closer. For CaSO<sub>4</sub> on the other hand, we observe something different. Here the shape is more complex. This is due to the anisotropic nature of sulfate which consists of one sulfur and 4 oxygen atoms. In the appendix, we show an illustration of calcium together with sulfate rotated at several angles in Fig. 18. We show the PMFs of several fixed orientations in Fig. 19 in the appendix. At different distances, different orientations are more favorable. This can lead to extended troughs as one favorable position replaces another. The recognizable peaks, on the other hand, observe the constant distance as before.

If we apply what we learned about the generic sodium chloride here to the previous chapters, a few things become clear. As the global minimum of the PMF is a lot deeper than for any other ion pair, we can safely assume that the attraction between either ion and the corresponding oppositely charged dipole of the water would be most attractive as well. This means a lot of water would hydrate the ions, creating empty spaces elsewhere in the box.

Lastly, the strong clustering can be explained by this. Ions “feel” each other across the whole slit and the force is strong enough for them to move towards each other on a scale of hundreds of picoseconds as we observed when looking at the diffusion.

## 5 Conclusion

In the present thesis, we have studied ionic salts by means of molecular simulations. In particular, atomistic models have been employed to characterize the behavior of nanoconfined electrolytes under the application of an electric field as well as to study the potential of mean force (PMF) experienced by different ions and under varying degrees of confinement.

Using grand canonical Monte Carlo simulations, we showed that water packs more tightly in a one-layer slit. However, a lot more pressure is needed for water and electrolytes to enter a nanoconfined slit than in a regular three-dimensional environment.

In a slit with two layers of water, we find that sodium chloride (NaCl) forms clusters at most densities. The currents are not dependent on the electric field and thus are not applicable as a memristor. On the contrary, divalent salts form clusters at different rates dependent on both, constant electric fields and density. As these clusters form, the electric current transmissible through the system decreases. These clusters neither form nor disappear instantaneously which implies memory effects can be observed at non-constant electric fields. As a consequence, a nanoconfined  $Z = 2$  electrolyte can be used as a memristor. This result has to be taken with a grain of salt, however, as the electric fields used are potentially too strong to be realistic. Future research should look at whether water experiences hydrolysis under the same conditions and if so whether the non-Ohmic effect also manifests at lower electric fields.

According to our expectations, we find that both monovalent and divalent salts observe diffusive behavior in the nanoconfined slit. We find that the rate of diffusion decreases for larger concentrations. However, the rate of diffusion fluctuates strongly between individual simulations, particularly for monovalent ions. Furthermore, the overall rate of diffusion is a lot lower for divalent ions. Therefore, we associate the decrease in movement with an increase of ions which are part of clusters. Consequently, we attribute the fluctuation to clusters forming with different frequencies and different sizes. For low concentrations, we expected the Nernst-Einstein equation would predict the conductivity of our system. However, at all concentrations and both valences, the conductivity is lower than the prediction based on the diffusion would suggest due to clustering and ion-ion interaction.

We also performed the, to our knowledge, first analysis of effective ion-ion interaction of nanoconfined electrolytes showing the long-range interactions of ions. By calculating the PMF of various salts, we demonstrated that valence is a crucial property of nanoconfined particles. For distances beyond 1 nm, different ion pairs' interaction patterns are barely distinguishable as long as they have the same valence and can be fully described by quasi 2D Coulombic (Q2D) interaction (see (2.12) and Ref. [11]). A general description of ions based on the Q2D potential is possible in systems where interaction occurs mostly at distances of more than 1 nm. Consequently, the specific shape of an ion is not important in such regimes.

However, at equilibrium conditions such as constant (or zero) electric fields, ions form clusters. At such length scales, the Q2D potential differs strongly from the measured PMF as it does not account for the finite size effects of water. The PMFs show steep potential wells at such distances which affects the formation and dissolution of ion pairs. Therefore, Q2D does not apply to the study of processes such as crystallization or even electric currents at a constant electric field. Small differences in Lennard-Jones (LJ) parameters lead to small differences in where potential wells lie and how deep they are. The differences between the depth of the potential or its absolute depth are smaller between NaCl and LiCl than they are for different force fields of NaCl. This could have a marginal effect on how many ion pairs form. For larger size differences, we see big differences in the PMFs. A generic divalent ion with the LJ parameters of NaCl had an effective interaction potential twice as deep as the larger calcium sulfate of equal valence as well as a more complex structure. Therefore, we expect the time it takes for clusters to break apart to be longer for the divalent ion. Future research should investigate whether these differences manifest and whether this has qualitative consequences.

In conclusion, this thesis highlights the importance of particle-based simulations in providing relevant qualitative and quantitative information in the study of nanoconfined ionic salts. The PMFs this thesis provides can be used to model a range of ion-ion interactions in nanoslits. Overall, nanoconfined electrolytes show very different behavior than their behavior under regular bulk would suggest.

## A Measure of Accuracy: R-squared

To measure the accuracy of the normal distribution, we define the coefficient of determination  $\bar{R}^2$

$$\bar{R}^2 = 1 - \frac{\sum_i (y_i - f_i)^2}{\sum_i (y_i - \bar{y})^2} \quad (\text{A.1})$$

with  $y_i$  being the measured values,  $f_i$  the ones predicted by the fit and  $\bar{y}$  the overall mean of the function. With this measure, we assure that measured values close to the mean do not differ greatly from our prediction. This is an appropriate measure in our case for two reasons. On the one hand, we want to ensure that our data is normally distributed around a single peak. On the other hand, at the center, often only one distribution informs about the probability distribution. At the edges, two distributions overlap meaning that variations here are less grave.

## B Different Orientations of Calcium Sulfate

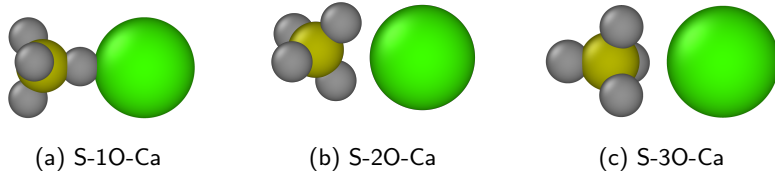


Figure 18: Illustration of Calcium Sulfate rotated to be separated by one, two or three oxygen atoms. The diameters of the spheres are based on the Lennard-Jones surfaces.

As mentioned in the main text,  $\text{CaSO}_4$  is not rotationally invariant. The structure of the PMF is more complex than that of the rotationally invariant ion pairs.

We want to look at several special orientations and look at where they contribute to potential. We consider three specific orientations to further explore the shape of the PMF of  $\text{CaSO}_4$ . Specifically, the cases where a given number of oxygen molecules is both equidistant and as close as possible to calcium. We refer to these three cases as S-1O-Ca, S-2O-Ca and S-3O-Ca, depending on how many oxygen atoms lie between the centers of mass (illustrated in Fig. 18). We show the PMFs of the three orientations (measured with CB) as well as the previously shown UI of a freely rotating pair in Fig. 19.

Those three potentials look very different from what we observe for the spring potential case in which  $\text{CaSO}_4$  is allowed to move freely. In some cases, these handpicked orientations have lower PMFs than the spring potential. This implies that at these positions, those orientations may be energetically more favorable yet unstable. That is if slightly perturbed it will move towards a different orientation.

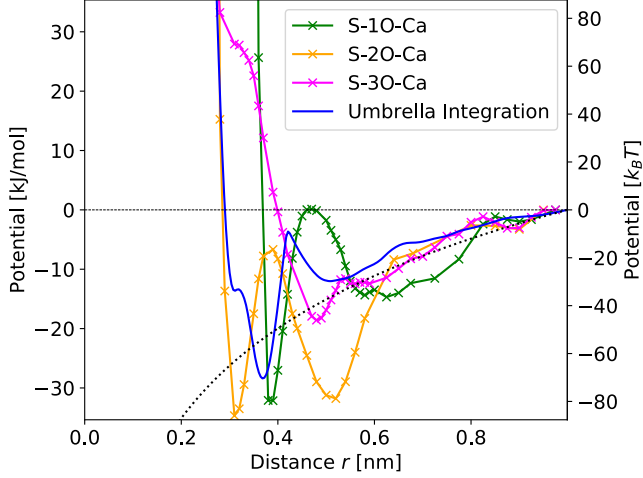


Figure 19: **PMF for  $\text{CaSO}_4$  at fixed orientations.** Orientations are illustrated in Fig. 18. New addition: S-2O-Ca, still needs to be beautified. Maybe add new data

In the case of S-1O-Ca, there the oxygen molecule sits on the line connecting the two centers of mass. Therefore, the LJ repulsion makes this position energetically unfavorable for a longer amount of time. Yet once this effect subsides, it has a negative oxygen atom right next to the center of mass of calcium. The PMF has its global minimum at the same position as measured for the case of Umbrella Integration. For the other, the hard shell repulsion fades at shorter distances. S-2O-Ca has two negatively charged oxygen atoms very close to the center of mass of calcium. Together those peaks

## C Comparing PMFs

Above, we showed how one can use umbrella integration to obtain PMFs from simulations where one attaches a spring potential. There are also other methods such as the weighted histogram analysis method (WHAM) [35]. We face the same issue as in WHAM, we have biased distributions  $p_k^s(r)$  and want to calculate the PMF. We use a different intermediate step, however, and instead of calculating the forces, we calculate the unbiased distributions  $p_k^u$ . With the unbiased distributions, we can then calculate the PMF  $U(r)$  as

$$U(r) = k_B T \ln p_k^u(r) \quad (\text{C.1})$$

The unbiased distributions can be obtained by iteratively solving these two equations

$$p_k^u(r) = \frac{\sum_l h_k(r)}{\sum_k N_k^{\text{Window}} \exp\left(\left[C_k - \omega_k(r)\right]/k_B T\right)} \quad (\text{C.2})$$

$$C_k = -k_B T \ln \int_r p_k^u(r) \exp\left(-\omega_k(r)/k_B T\right). \quad (\text{C.3})$$

Here,  $h_k(r)$  stands for the counts at bin  $k$  and distance  $r$ ,  $N_k^{\text{Window}}$  the total number of counts in a window and  $C_k$  for the estimated offset between windows. Furthermore,  $\omega_k$  is the spring potential that we attach to each window. We use this method

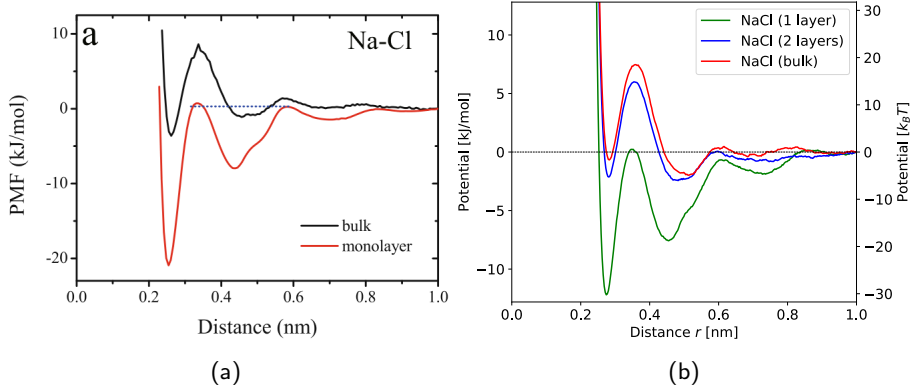


Figure 20: **PMF of NaCl using WHAM.** The plot in (a) is from Fig. 5a in Ref. [9] whereas (b) is made with the same data as shown in Fig. 15.

to replicate the results of Ref. [9] and show both their and our results in Fig. 20<sup>7</sup>. We see that these two figures match fairly well both for the single-layer case as well as the bulk case. We use different LJ parameters for sodium which ought to explain the quantitative differences. If we compare this to what we see in Fig. 15, the difference is striking, especially at longer distances.

We did not feed information into the system on how the volume of bins differed (see discussion in chapter 3.7). Bins are first spherical and later cylindrical. This means that the bins are first divided by a volume term scaling with  $r^3$  and later  $r^2$ . After inserting  $p_k^u(r)$  into Eq. (C.1), this means the earlier potential and the later differ by an extra term of  $\mathcal{O}(\log r)$ . At this length scale, the Q2D potential also scales with  $\mathcal{O}(\log r)$ . We assume that those two contributions cancel each other, leading to a representation that implies that there is no long-range interaction.

<sup>7</sup>Unlike in some of the PMFs shown above, there are no transformations applied after executing the algorithm

## D Pressures

Now, doing away with the grand canonical simulations, we move to a larger system slit system with an in-plane area of  $L_x \times L_y = 10 \text{ nm} \times 10 \text{ nm}$  (All numerical parameters are also listed in Tab. 5). We now look at the effect of the water from the opposite perspective. We insert a fixed amount of water into the slit and measure the resulting pressure. This pressure is highly anisotropic as the movement in the out-of-plane dimension is constrained with a slit width of  $h = 1 \text{ nm}$ . From here onwards, we use idealized walls by using an LJ93 potential. We inserted between 2100 and 2500 water molecules which corresponds to a density between 21 and  $25 \text{ nm}^{-2}$ . For the time evolution, we used the velocity Verlet algorithm and added a Nosé-Hoover Thermostat, just like in the previous simulations. We were also curious about the influence different salts have on pressure. Thus, besides pure water, we considered a range of different ions such as  $\text{CaCl}_2$  and  $\text{LiCl}$  as well as mono-, di- and trivalent  $\text{NaCl}$  and the case without ions. Of each, we insert 25 ion pairs (triplets in the case of  $\text{CaCl}_2$ ), which corresponds to an ion concentration of 0.63 mol/l. The system is initialized by inserting the water molecules and salt ions at random. As some particles may be physically close, the forces they experience may be very large. We bring the system to equilibrium by alternating between two methods. The so-called “fixed-*NVE*” method updates particles with the velocity Verlet algorithm with a maximum velocity per time step. This means that the strong forces on unreasonably close particles cannot shoot particles out of the box. The other method is an *NVT* ensemble with a very small time step. Then the system is brought to equilibrium by alternating between fixed-*NVE* at a time step of 1 fs and *NVT* simulations with very low yet increasing time steps (which start at  $1 \times 10^{-6}$  fs).

We run each simulation for 1 ns and measure the pressure of the system every 0.1 ps. We separate those measurements in chunks of 0.25 ns and calculate the averages. Of those, we then again calculate the average and the standard error of the mean. This value is slightly larger than the overall standard error of the mean yet still very small compared to the slope. From this, we can deduce that the values we report are fairly accurate even if the pressure fluctuates strongly on very short time scales.

Parameters	MD: Pressure
$L_x \times L_y$	$10 \times 10 \text{ nm}^2$
$h$ : Slit	1 nm
Time step $\Delta t$	1 fs
Run time	1 ns
Ion pairs $N_{\text{ions}}$	25
Electric Field $E$	0
Water Molecules $\rho$	$21 \text{ nm}^{-2}$ to $25 \text{ nm}^{-2}$
Wall	LJ93 based on Carbon

Table 5: List of simulation parameters in pressure analysis

In Fig. 21(a), we show the average pressure for sodium chloride in all three dimensions as a function of the water density per slit area  $\rho$ . For all three, we see a monotonic and seemingly linear relationship between water density and pressure. In the out-of-plane dimension, we observe a highly positive pressure at all times. If this pressure were not there, this aquatic solution could exist in this shape even without constraining walls. The in-plane pressure is negative for lower densities and rises to positive values for larger densities. Due to the periodic boundary conditions, the plane is effectively infinite. A negative pressure implies that there is space to be filled. If this slit was attached to a water reservoir, it would stream into the slit. For positive pressures, the opposite is the case. Experimentally, either a closed system or a system with a fixed reservoir would be realizable. In both cases, negative pressures would be hard to realize. In a closed box, one would have to enforce a partial vacuum. If attached to a reservoir, water (with/or without additional ions) would stream into the slit. However, after a finite amount of time, this slit would be filled. A positive pressure is more easily realized by attaching a reservoir with a pump or inserting a large amount of water (and/or ions) and then sealing the box.

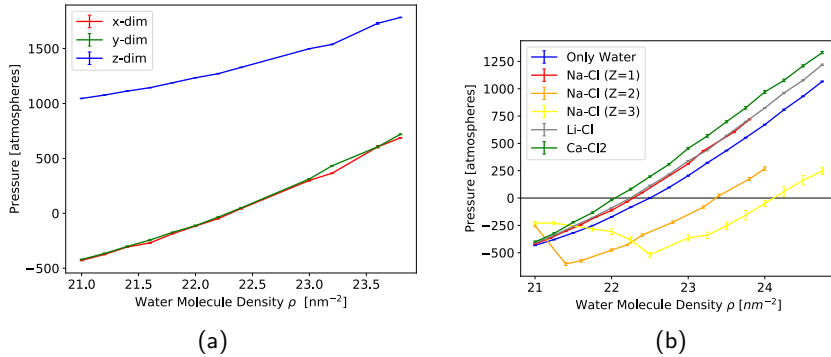


**Figure 21: Pressure at different water molecule densities.** (a) We measure the Pressure in the in-plane (x,y) and normal (z) dimension of a slit of  $10 \times 10 \times 1 \text{ nm}^3$ . This slit is filled with 25 NaCl ion pairs. (b) The in-plane pressure of various salts (also 25 ion pairs), as well as generic Na-Cl with doubled and tripled charge. The non-monotonous areas correspond to simulations in which holes formed.

Since we look at a range of different salts, we want to see what impact they have on the in-plane pressure. As we see in Fig. 21b, for the ‘real’ salts as well as water, we see curves with very similar slopes. An electrolyte of water with sodium chloride and lithium chloride can barely be distinguished. Water without any salts inserted has a lower pressure than with the salts inserted. Calcium chloride has the highest pressure. Qualitatively, this can be explained by the different numbers of particles in the system. The number of water molecules is given by the x-axis, yet NaCl and

LiCl represent an extra of 50 and CaCl<sub>2</sub> an extra of 75 particles. They all take up space and press against each other, leading to higher pressure.

What happens to the generic ions is more interesting, which we also show in Fig. 21 (b). Unlike in the other cases, pressure decreases/stays flat for lower densities. Only at higher water molecule densities do they transition to the monotonic regime. What we observe at lower pressures, are vast and easily visible holes in the water (compare Fig. 22). Showing that the slit wasn't saturated by the number of water molecules. The constant pressure is an artifact of the way it is calculated. As there effectively is a liquid-vapor interface, we ought to consider the pressure of the vapor and the liquid separately. The pressure, however, is calculated over the whole area.

Using the knowledge we will gain about the PMFs later on, we see that the combination of a small LJ diameter and high charge attracts a lot of water. Thus, the water condenses around the ions creating additional negative pressure in the areas not occupied by the ions.

Furthermore, applying the above described Maxwell relation (see Eq. (4.1)), we can calculate the differential in chemical potential  $\mu$ . Given the area density multiplied with the slit height  $h = 1 \text{ nm}$ , we can solve for  $\mu$  and obtain roughly a difference of 6 kcal/mol for the conventional salts. For the generic salts, it is roughly a quarter of that.

## E Additional Figures

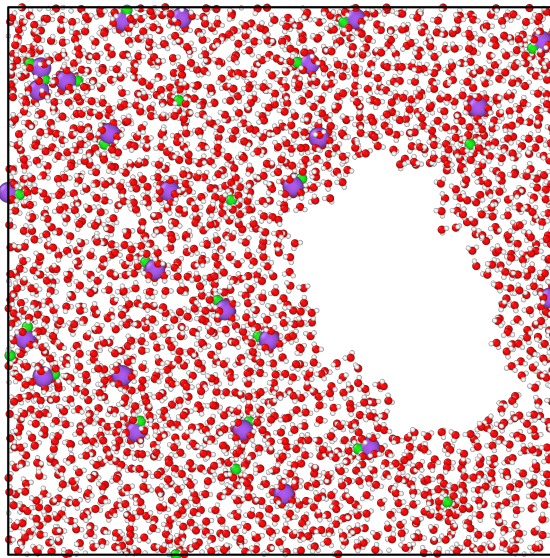


Figure 22: **Example of insufficient water molecule density.** Generic ion with valence  $Z = 3$  at density  $\rho = 21 \text{ nm}^{-2}$ .

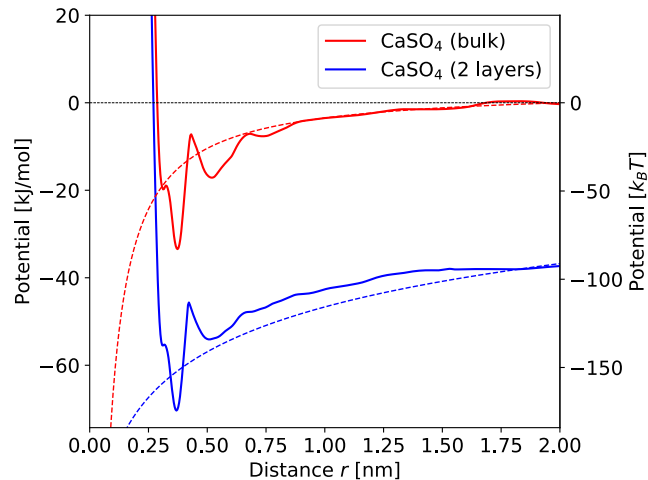


Figure 23: **PMFs of  $\text{CaSO}_4$  in bulk and slit.** The slit is of dimension  $10 \times 10 \times 1 \text{ nm}^3$  and has a water molecule number density of  $23.2 \text{ nm}^{-3}$  whereas the bulk system is of size  $5 \times 5 \times 5 \text{ nm}^3$  and has a mass density of  $997 \text{ kg/m}^3$ .

The PMFs were calculated with Umbrella Integration and then transformed according to Eq. (4.3). The Q2D potential as described in Eq. (2.12) and the Coulomb potential as in Eq. (2.2).

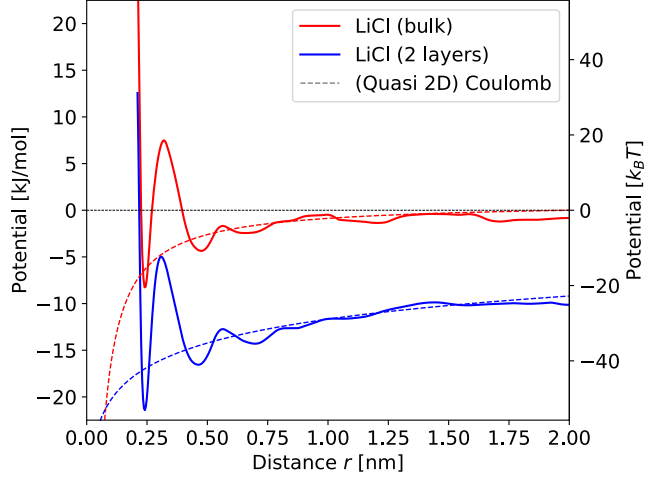


Figure 24: **PMFs of LiCl in the bulk and slit.** The slit is of dimension  $10 \times 10 \times 1 \text{ nm}^3$  and has a water molecule number density of  $23.2 \text{ nm}^{-3}$  whereas the bulk system is of size  $5 \times 5 \times 5 \text{ nm}^3$  and has a mass density of  $997 \text{ kg/m}^3$ .

The PMFs were calculated with Umbrella Integration and then transformed according to Eq. (4.3). The the Q2D potential as described in Eq. (2.12) and the Coulomb potential as in Eq. (2.2).

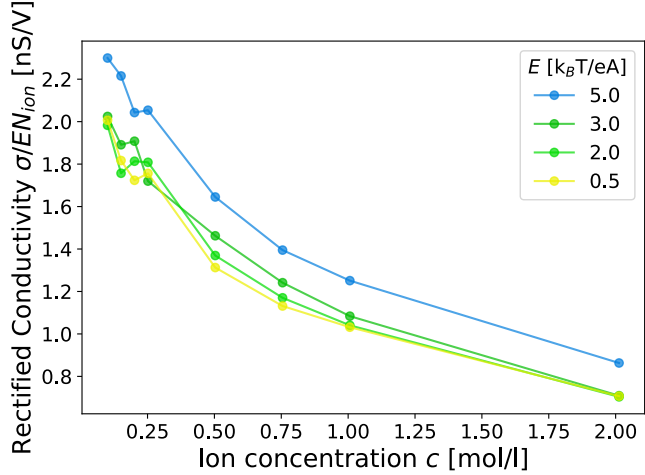


Figure 25: **Normalized conductivity for different electric fields and ion concentrations.** Electric Conductivity is divided by the number of ions  $N_{ion}$  and the electric field applied. Ions have valence  $Z = 1$ . Simulation ran for 2 ns.

## References

- [1] Lev Landau. The theory of phase transitions. *Nature*, 138(3498):840–841, 1936.
- [2] Eduardo Fradkin. Critical behavior of disordered degenerate semiconductors. ii. spectrum and transport properties in mean-field theory. *Physical review B*, 33(5):3263, 1986.
- [3] Kostya S Novoselov, Andre K Geim, Sergei V Morozov, De-eng Jiang, Yanshui Zhang, Sergey V Dubonos, Irina V Grigorieva, and Alexandr A Firsov. Electric field effect in atomically thin carbon films. *science*, 306(5696):666–669, 2004.
- [4] Andre K Geim and Konstantin S Novoselov. The rise of graphene. In *Nanoscience and technology: a collection of reviews from nature journals*, pages 11–19. World Scientific, 2010.
- [5] Deji Akinwande, Christopher J Brennan, J Scott Bunch, Philip Egberts, Jonathan R Felts, Huajian Gao, Rui Huang, Joon-Seok Kim, Teng Li, Yao Li, et al. A review on mechanics and mechanical properties of 2d materials—graphene and beyond. *Extreme Mechanics Letters*, 13:42–77, 2017.
- [6] Andre K Geim. Exploring two-dimensional empty space, 2021.
- [7] Hiroaki Yoshida, Vojtěch Kaiser, Benjamin Rotenberg, and Lydéric Bocquet. Driplons as localized and superfast ripples of water confined between graphene sheets. *Nature communications*, 9(1):1–9, 2018.
- [8] Ashok Keerthi, Andre K Geim, A Janardanan, Aidan P Rooney, Ali Esfandiar, S Hu, Sidra Abbas Dar, Irina V Grigorieva, Sarah J Haigh, FC Wang, et al. Ballistic molecular transport through two-dimensional channels. *Nature*, 558(7710):420–424, 2018.
- [9] Wenhui Zhao, Yunxiang Sun, Weiduo Zhu, Jian Jiang, Xiaorong Zhao, Dong-dong Lin, Wenwu Xu, Xiangmei Duan, Joseph S Francisco, and Xiao Cheng Zeng. Two-dimensional monolayer salt nanostructures can spontaneously aggregate rather than dissolve in dilute aqueous solutions. *Nature communications*, 12(1):1–8, 2021.
- [10] Hui Zhang, Bo Liu, Mao-See Wu, Kun Zhou, and Adrian Wing-Keung Law. Transport of salty water through graphene bilayer in an electric field: A molecular dynamics study. *Computational Materials Science*, 131:100–107, 2017.
- [11] Paul Robin, Nikita Kavokine, and Lydéric Bocquet. Modeling of emergent memory and voltage spiking in ionic transport through angstrom-scale slits. *Science*, 373(6555):687–691, 2021.
- [12] Ke Zhou, Shuping Jiao, Yan Chen, Huasong Qin, and Yilun Liu. Reduced ionic conductivity but enhanced local ionic conductivity in nanochannels. *Langmuir*, 37(43):12577–12585, 2021.

- [13] Haolan Tao, Gong Chen, Cheng Lian, Honglai Liu, and Marc-Olivier Coppens. Multiscale modeling of ion transport in porous electrodes. *AIChE Journal*, 68(4):e17571, 2022.
- [14] R Eisenschitz and Fritz London. Über das verhältnis der van der waalsschen kräfte zu den homöopolaren bindungskräften. *Zeitschrift für Physik*, 60(7):491–527, 1930.
- [15] Hendrik Antoon Lorentz. Ueber die anwendung des satzes vom virial in der kinetischen theorie der gase. *Annalen der physik*, 248(1):127–136, 1881.
- [16] Daniel Berthelot. Sur la détermination rigoureuse des poids moléculaires sentent par rapport à la loi de mariotte. *Compt. Rendus*, 126:954–956, 1898.
- [17] Simao P Pinho and Eugénia A Macedo. Solubility of nacl, nabr, and kcl in water, methanol, ethanol, and their mixed solvents. *Journal of Chemical & Engineering Data*, 50(1):29–32, 2005.
- [18] René van Roij. Soft condensed matter theory (lecture notes), 2021.
- [19] H. Jalali, H. Ghorbanfekr, Ilyar Hamid, M. Neek-Amal, R. Rashidi, and F. M. Peeters. Out-of-plane permittivity of confined water. *Phys. Rev. E*, 102:022803, Aug 2020.
- [20] Elton JG Santos and Efthimios Kaxiras. Electric-field dependence of the effective dielectric constant in graphene. *Nano letters*, 13(3):898–902, 2013.
- [21] Yan Levin. Electrostatic correlations: from plasma to biology. *Reports on progress in physics*, 65(11):1577, 2002.
- [22] A. P. Thompson, H. M. Aktulga, R. Berger, D. S. Bolintineanu, W. M. Brown, P. S. Crozier, P. J. in 't Veld, A. Kohlmeyer, S. G. Moore, T. D. Nguyen, R. Shan, M. J. Stevens, J. Tranchida, C. Trott, and S. J. Plimpton. LAMMPS - a flexible simulation tool for particle-based materials modeling at the atomic, meso, and continuum scales. *Comp. Phys. Comm.*, 271:108171, 2022.
- [23] HJC Berendsen, JR Grigera, and TP Straatsma. The missing term in effective pair potentials. *Journal of Physical Chemistry*, 91(24):6269–6271, 1987.
- [24] Jean-Paul Ryckaert, Giovanni Ciccotti, and Herman JC Berendsen. Numerical integration of the cartesian equations of motion of a system with constraints: molecular dynamics of n-alkanes. *Journal of computational physics*, 23(3):327–341, 1977.
- [25] Hyman D Gesser. *Applied chemistry: a textbook for engineers and technologists*. Springer, 2002.
- [26] Loup Verlet. Computer" experiments" on classical fluids. i. thermodynamical properties of lennard-jones molecules. *Physical review*, 159(1):98, 1967.

- [27] Daan Frenkel and Berend Smit. *Understanding molecular simulation: from algorithms to applications*, volume 1. Elsevier, 2001.
- [28] William C Swope, Hans C Andersen, Peter H Berens, and Kent R Wilson. A computer simulation method for the calculation of equilibrium constants for the formation of physical clusters of molecules: Application to small water clusters. *The Journal of chemical physics*, 76(1):637–649, 1982.
- [29] Michael P Allen and Dominic J Tildesley. *Computer simulation of liquids*. Oxford university press, 1987.
- [30] Sandia National Laboratories. LAMMPS Manual: kspace modify command, 2022.
- [31] In-Chul Yeh and Max L Berkowitz. Ewald summation for systems with slab geometry. *The Journal of chemical physics*, 111(7):3155–3162, 1999.
- [32] Farid F Abraham and Y Singh. The structure of a hard-sphere fluid in contact with a soft repulsive wall. *The Journal of Chemical Physics*, 67(5):2384–2385, 1977.
- [33] Johannes Kästner. Umbrella sampling. *Wiley Interdisciplinary Reviews: Computational Molecular Science*, 1(6):932–942, 2011.
- [34] MM Locarnini, AV Mishonov, OK Baranova, TP Boyer, MM Zweng, HE Garcia, D Seidov, Kw Weathers, Cr Paver, I Smolyar, et al. World ocean atlas 2018, volume 1: Temperature. 2018.
- [35] Shankar Kumar, John M Rosenberg, Djamal Bouzida, Robert H Swendsen, and Peter A Kollman. The weighted histogram analysis method for free-energy calculations on biomolecules. i. the method. *Journal of computational chemistry*, 13(8):1011–1021, 1992.